

Implications of portal vector-like lepton on associated Higgs production at a multi-TeV muon collider

Krishna Tewary^{a,*}, Sanjoy Biswas^{a,†}, and Shivam Verma^{b,‡}

^a*Department of Physics, Ramakrishna Mission Vivekananda Educational and Research Institute, Belur Math, Howrah 711202, India.*

^b*Theoretical Physics Division, Physical Research Laboratory, Shree Pannalal Patel Marg, Ahmedabad - 380009, Gujarat, India.*

Abstract

We have explored a *portal vector-like lepton* (pVLL) extension of the Standard Model (SM) and studied its implications for Higgs and vector-boson associated production (hV , with $V = Z$ -boson or dark photon) at a future muon collider facility. We show that while the $\mu^+ \mu^- \rightarrow hZ$ production rate remains close to its SM prediction in a wide range of parameter space, the rate for $\mu^+ \mu^- \rightarrow h\gamma_d$ can be substantially enhanced owing to the *non-decoupling nature* of the interaction involving the heavy lepton, the muon and the dark photon. We demonstrate that the $h\gamma_d$ production rate can exceed the corresponding hZ rate by a factor of 1–100 within the *perturbative unitarity limit*, making it a promising channel for probing Higgs interactions and potential new physics effects.

Furthermore, this process can also be used to constrain the dark photon mass (m_{γ_d}) and/or the dark gauge coupling (g_d) consistent with the current muon $g - 2$ measurements within the pVLL framework. We perform a detailed collider analysis of the $h\gamma_d$ process in the $b\bar{b} +$ missing energy final state. A 2σ exclusion limit for m_{γ_d} up to 80 GeV is obtained assuming $g_d = 0.05$, $\sin \theta_L = 4 \times 10^{-5}$, $\sin \theta_s = 0.05$, for a heavy lepton mass ~ 3 TeV at a 3 TeV muon collider with an integrated luminosity of 1 ab^{-1} .

^{*}krishna.tewary.phy22@gm.rkmvu.ac.in, krishnatewary3@gmail.com

[†]sanjoy.phy@gm.rkmvu.ac.in, sanjoyhri@gmail.com

[‡]shivamverma@prl.res.in, shivam.59910103@gmail.com

1 Introduction

The discovery of the Higgs boson [1, 2] marks a remarkable triumph of theoretical and experimental particle physics. To probe its properties with greater precision, however, we require an abundant production of Higgs bosons at high-energy (HE) and high-luminosity (HL) facilities such as the Large Hadron Collider (LHC) and future collider experiments. Higgs production in association with a gauge boson is a well-studied process at lepton colliders [3–7], both in past experiments [8, 9] and in proposed future facilities [10–13]. The presence of new physics, particularly, scenarios predicting vector-like leptons (VLLs), can significantly alter the associated Higgs production cross section at lepton colliders—either through modified Higgs couplings, the appearance of new diagrams, or both. Moreover, such scenarios may open up additional Higgs production channels with enhanced rates. In this work, we explore the implications of VLLs acting as portal matter on the Higgs production cross section at a future muon collider.

VLLs constitute a simple yet well-motivated extension of the Standard Model (SM) of particle physics. VLL extension of the SM has been studied extensively in the literature in the context of various anomalies, including the muon $g - 2$, the W -boson mass, the Cabibbo angle anomaly, and dark matter phenomenology [14–27]. They naturally arise in a variety of theoretical frameworks [28–33], including grand unified theories, models addressing the Higgs mass hierarchy problem, and constructions inspired by string theory. The search for VLLs at collider experiments remains an active area of investigation, including both prompt and long-lived signatures, primarily in SM final states [34–36]. VLL is also a potential candidate to search for at the future colliders such as future pp , e^+e^- , muon collider [37–41].

In recent years, the idea of VLLs as portal matter [18, 42–44] or portal VLLs (pVLLs) has gained significant interest owing to their rich phenomenology, their ability to evade existing collider constraints, and their potential connection to the dark sector, particularly dark matter phenomenology [45, 46].

In this work, we consider an extension of the Standard Model (SM) with an $SU(2)$ -singlet VLL that transforms under both the SM hyper-charge group $U(1)_Y$ and an additional abelian dark gauge group $U(1)_D$ [18, 42–44]. The gauge boson associated with $U(1)_D$ is referred to as the dark photon (γ_d). The model also contains an additional complex scalar field, singlet under the SM gauge group but carrying non-zero $U(1)_D$ charge. The full gauge symmetry, $SU(3)_C \times SU(2)_L \times U(1)_Y \times U(1)_D$, is spontaneously broken to $SU(3)_C \times U(1)_{EM}$ through the non-vanishing vacuum expectation values (VEVs) of the SM Higgs doublet and the dark scalar. The VEV of the dark scalar not only generates the dark photon mass but also induces mixing between the pVLL and SM leptons through a Yukawa-type portal interaction. The $U(1)_Y$ hypercharge assignment of the pVLL considered here corresponds to an electric charge of -1 , and it is allowed to mix only with one generation of SM charged leptons in order to evade stringent bounds from lepton-flavor violation. In this work, we focus on pVLL mixing with the second-generation charged lepton.

An important feature of this model is that the right-handed second generation charged lepton (μ'_R) and the pVLL (μ'_p) carry identical $SU(2)_L \times U(1)_Y$ charges. Consequently, any rotation between μ'_R and μ'_{p_R} preserves the diagonal structure of the Z -boson couplings, ensuring that no $\mu_R - \mu_{p_R} - Z$ interaction arises after transforming to the mass basis. In contrast, since the muon is uncharged under $U(1)_D$, such a rotation induces an off-diagonal $\mu_R - \mu_{p_R} - \gamma_d$ coupling, suppressed by $\sin \theta_R$, the sine of the corresponding mixing angle. One can have a sizable value of $\sin \theta_R \sim 0.1$ for heavy muon mass \sim a few TeV even when the mixing angle ($\sin \theta_L$) involving the corresponding left-chiral fermions is kept at a tiny value $\sim 10^{-5}$.

We explore this *non-decoupling* effect within the limit of *perturbative unitarity* at the proposed future muon collider, focusing on Higgs production in association with a vector boson ($\mu^+\mu^- \rightarrow hV$ with $V = Z, \gamma_d$). The muon collider [47–49] is envisioned as a high-energy circular lepton collider that combines the clean experimental environment of lepton collisions with access to multi-TeV center-of-mass energies (\sqrt{s}), in contrast to circular e^+e^- machines. It is designed to operate at energy stages from an initial 3 TeV to 10 TeV (or higher), corresponding to circumferences of about 4.5 km and 10 km, respectively, with expected peak integrated luminosities of 1 ab^{-1} at $\sqrt{s} = 3 \text{ TeV}$ and 10 ab^{-1} at $\sqrt{s} = 10 \text{ TeV}$ [50].

We have shown that while the hZ production cross section remains essentially unchanged from

the SM prediction, the $h\gamma_d$ production rate can be significant even for very small $\sin\theta_L$, owing to the non-decoupling effect. In this scenario, the dark photon is treated as an invisible particle¹. We analyze this process in the $b\bar{b}$ *plus missing energy* final state at $\sqrt{s} = 3$ and 10 TeV muon colliders, where the $b\bar{b}$ system is highly boosted due to the $2 \rightarrow 2$ kinematics and large center-of-mass energy. The dominant SM backgrounds to this channel are processes leading to $b\bar{b}\nu\bar{\nu}$ final state, with $h\nu\bar{\nu}$ and $Z\nu\bar{\nu}$ accounting for more than 90% of the total cross section. We demonstrate that the requirement of jet substructure, together with additional kinematic selections such as missing energy and the $b\bar{b}$ invariant mass, can efficiently suppress these backgrounds.

The main highlight of this work is that the $h\gamma_d$ process not only yields a higher Higgs production rate than hZ production at a muon collider, but also offers a noble way to explore dark photons in the mass range 10–100 GeV, independent of the gauge kinetic mixing parameter (ϵ) [51–54]. This is because of the fact that the muon–heavy muon–Higgs vertex is sensitive to the dark photon mass (m_{γ_d}) and the dark gauge coupling (g_d). Consequently, the absence of any observable enhancement in Higgs production along with missing energy at a muon collider would imply a stringent limit on m_{γ_d} or g_d , for fixed values of other relevant model parameters. We illustrate this using several representative benchmark points and show that, even for fermion mixing angle as small as $\sim 10^{-6}$ and heavy muon masses in the range 1–3 TeV, a wide range of dark photon masses can be excluded. We illustrate that a substantial region of the parameter space consistent with current measurement of muon $g - 2$ can be probed at the future muon collider using our analysis.

The remainder of the manuscript is organized as follows. In Section 2, we present the theoretical framework considered in this work to illustrate the impact of portal VLLs on associated Higgs production at muon collider, along with a discussion of relevant constraints on the model parameters. Section 3 describes the collider analysis of Higgs production in association with a vector boson. The results of our analysis are presented in Section 4, and finally we conclude in Section 5.

2 Theoretical Framework

We consider a framework in which the Standard Model is extended by a vector-like lepton, singlet under $SU(3)_C \times SU(2)_L$ with $U(1)_Y$ hypercharge -1. The VLL plays the role of a portal matter, linking the visible SM sector with a dark sector. A simplified realization of such a scenario is to have a VLL transforming non-trivially under an additional local $U(1)_D$ symmetry of the dark sector with corresponding gauge boson referred to as the dark photon (γ_d). The dark photon acquires mass through spontaneous breaking of $U(1)_D$, achieved by introducing a complex scalar field Φ_d which is a singlet under the SM gauge group but charged under $U(1)_D$. Furthermore, if Φ_d carries the same $U(1)_D$ charge as the pVLL, a Yukawa-type portal interaction $\omega_f \Phi_d \bar{\mu}'_{pL} \mu'_R$ is permitted. The Yukawa interaction reduces to a bilinear term between the pVLL and the SM lepton once Φ_d gets a non-zero VEV. In this work, we focus on the case where the pVLL mixes with the second-generation charged lepton only to avoid constraints coming from flavor violating observables. The assignment of charge of the relevant field content is presented in Table 1.

¹This will be the case if the dark photon couples to dark matter particle and predominantly decays to invisible final state.

Fields	$SU(3)_C$	$SU(2)_L$	Y	Y_d
μ'_R	1	1	-1	0
$L_L = \begin{pmatrix} \nu_{\mu'_L} \\ \mu'_L \end{pmatrix}$	1	2	-1/2	0
Φ	1	2	1/2	0
μ'_p	1	1	-1	1
Φ_d	1	1	0	1

Table 1: Representation of relevant fields and their $U(1)$ charge assignment under the extended gauge group.

In Table 1, μ'_R and L_L represent the second-generation SM right-handed charged lepton and left-handed lepton doublet, respectively, and Φ corresponds to the SM complex scalar field doublet. The additional VLL singlet under $SU(2)_L$ is represented by μ'_p . Φ_d is the complex scalar field that does not carry charges under the SM gauge group. All fields are expressed in their interaction basis. The SM Lagrangian now will be extended with new terms coming from the effect of the BSM interactions we have considered in our model.

The complete Lagrangian of the model invariant under $SU(3)_C \times SU(2)_L \times U(1)_Y \times U(1)_D$ can be expressed as

$$\mathcal{L} = \mathcal{L}_{\text{Gauge}} + \mathcal{L}_{\text{Scalar}} + \mathcal{L}_{\text{Fermions}} + \mathcal{L}_{\text{Yukawa}} \quad (1)$$

where $\mathcal{L}_{\text{Gauge}}$, $\mathcal{L}_{\text{Scalar}}$, $\mathcal{L}_{\text{Fermions}}$ are part of the full Lagrangian containing gauge invariant kinetic terms involving the gauge fields, scalar fields including corresponding scalar potential, and fermion fields including the mass term of the pVLL, respectively. Finally, $\mathcal{L}_{\text{Yukawa}}$ represents the trilinear Yukawa interactions involving scalar and fermions.

In particular, the gauge sector of the theory is given by

$$\mathcal{L}_{\text{Gauge}} = -\frac{1}{4}G_{\mu\nu}^a G^{a,\mu\nu} - \frac{1}{4}W_{\mu\nu}^i W^{i,\mu\nu} - \frac{1}{4}B_{\mu\nu} B^{\mu\nu} - \frac{1}{4}B_{d,\mu\nu} B_d^{\mu\nu} + \frac{\varepsilon}{2\cos\theta_w} B_{d,\mu\nu} B^{\mu\nu}, \quad (2)$$

where $G_{\mu\nu}^a$ denotes the QCD field strength tensor with $a = 1, \dots, 8$ labeling the adjoint of $SU(3)_C$, $W_{\mu\nu}^i$ ($i = 1, 2, 3$) are the field strength tensors of $SU(2)_L$, $B_{\mu\nu}$ corresponds to the $U(1)_Y$ hypercharge, and $B_{d,\mu\nu}$ is the field strength tensor of the dark $U(1)_D$.

The scalar-sector Lagrangian is

$$\mathcal{L}_{\text{Scalar}} = |D_\mu \Phi|^2 + |D_\mu \Phi_d|^2 - V(\Phi, \Phi_d), \quad (3)$$

with the scalar potential

$$V(\Phi, \Phi_d) = -\mu_h^2 |\Phi|^2 - \mu_{h_d}^2 |\Phi_d|^2 + \lambda_h |\Phi|^4 + \lambda_{h_d} |\Phi_d|^4 + \lambda_{hh_d} |\Phi|^2 |\Phi_d|^2. \quad (4)$$

The symmetry breaking condition and boundedness of the potential require $\mu_h^2, \mu_{h_d}^2 > 0$ and $(\lambda_h \lambda_{h_d} - \lambda_{hh_d}^2), \lambda_h, \lambda_{h_d} > 0$. The field configurations of Φ and Φ_d at the minima of the scalar potential in unitary gauge is given by

$$\Phi = \begin{pmatrix} 0 \\ \frac{v_{\text{EW}} + h_1}{\sqrt{2}} \end{pmatrix}, \quad \Phi_d = \frac{1}{\sqrt{2}}(v_d + h_2). \quad (5)$$

where h_1 and h_2 denote the fluctuation around the minimum field configurations and v_{EW} and v_d represent the VEV of the respective scalar fields². We denote the fields in the mass basis by h and

²The mass of the dark photon accordingly is given by $m_{\gamma_d} = g_d v_d$.

h_d which correspond to the observed Higgs and the hypothetical dark Higgs fields, respectively. The physical scalar fields (h , h_d) are related to the (h_1 , h_2) by the following unitary transformation

$$\begin{pmatrix} h \\ h_d \end{pmatrix} = \begin{pmatrix} \cos \theta_s & -\sin \theta_s \\ \sin \theta_s & \cos \theta_s \end{pmatrix} \begin{pmatrix} h_1 \\ h_2 \end{pmatrix} \quad (6)$$

Here, θ_s is the scalar mixing angle.

The expression for $\mathcal{L}_{\text{Fermion}}$ and $\mathcal{L}_{\text{Yukawa}}$ appearing in Eq. (1) involving second generation leptons and pVLL consistent with gauge symmetry are given by

$$\mathcal{L}_{\text{Fermions}} \supset i[\bar{L}_L \not{D} L_L + \bar{\mu}'_R \not{D} \mu'_R + \bar{\mu}'_p \not{D} \mu'_p] - m_{\mu'_p} \bar{\mu}'_p \mu'_p. \quad (7)$$

$$\mathcal{L}_{\text{Yukawa}} \supset -y_m \bar{L}_L \Phi \mu'_R - \omega_f \Phi_d \bar{\mu}'_p \mu'_R + \text{H.c.} \quad (8)$$

The mixing between μ' and μ'_p is generated once the dark Higgs assumes non-zero VEV. After symmetry breaking, the mass matrix in the interaction basis μ' and μ'_p takes the form

$$\mathcal{M} = \begin{pmatrix} \frac{y_m v_{\text{EW}}}{\sqrt{2}} & 0 \\ \frac{\omega_f v_d}{\sqrt{2}} & m_{\mu'_p} \end{pmatrix} \quad (9)$$

The mass eigenbasis μ and μ_p in which the mass matrix is diagonal, represent the physical muon and the corresponding heavy muon partner, respectively. The mass eigenbasis and the interaction basis are connected by the following bi-unitary transformation,

$$\begin{pmatrix} \mu \\ \mu_p \end{pmatrix}_{L,R} = \begin{pmatrix} \cos \theta_{L,R} & -\sin \theta_{L,R} \\ \sin \theta_{L,R} & \cos \theta_{L,R} \end{pmatrix} \begin{pmatrix} \mu' \\ \mu'_p \end{pmatrix}_{L,R} \quad (10)$$

where, $\theta_{L,R}$ is the mixing angle between the left (right) chiral muon and the corresponding muon partner with same chirality.

The model parameters y_m , ω_f , $m_{\mu'_p}$ appearing in the Lagrangian of Eq. (7) and (8) can be expressed in terms of the physical parameters m_μ , m_{μ_p} and $\sin \theta_L$ as

$$y_m = \frac{\sqrt{2}}{v_{\text{EW}}} m_{\mu_p} D \quad (11a)$$

$$\omega_f = \frac{m_{\mu_p} (1 - \frac{m_\mu^2}{m_{\mu_p}^2})}{\sqrt{2} v_d D} \sin 2\theta_L \quad (11b)$$

$$m_{\mu'_p} = \frac{m_\mu}{D} \quad (11c)$$

where D is a dimensionless quantity given by $D = \sqrt{\frac{m_\mu^2}{m_{\mu_p}^2} \cos^2 \theta_L + \sin^2 \theta_L}$.

The absolute value of the sine of the mixing angle between the left chiral second generation charged lepton and the pVLL is expressed as

$$|\sin \theta_L| = \frac{1}{2} \sqrt{\frac{2m_{\mu_p}^2 - 2m_\mu^2 - \omega_f^2 v_d^2}{m_{\mu_p}^2 - m_\mu^2}} \left(1 - \sqrt{1 - \frac{8\omega_f^2 v_d^2 m_\mu^2}{(2m_{\mu_p}^2 - 2m_\mu^2 - \omega_f^2 v_d^2)^2}} \right) \quad (12)$$

The reality of $\sin \theta_L$ requires

$$|\omega_f| < \sqrt{2} \frac{(m_{\mu_p} - m_\mu)}{v_d} \quad (13)$$

On the other hand, the perturbative unitarity [55] demands

$$|\omega_f| < 4\sqrt{2\pi} \quad (14)$$

These two conditions can be integrated as

$$|\omega_f| < \sqrt{2} \min\left(\frac{m_{\mu_p} - m_\mu}{v_d}, 4\sqrt{\pi}\right) \quad (15)$$

This framework naturally gives rise to three portal interactions connecting the visible and dark sectors: the *gauge kinetic mixing*, *Yukawa*, and *scalar* portals. In particular, gauge kinetic mixing between the SM $U(1)_Y$ and dark $U(1)_D$ arises at one loop and is strongly constrained by low-energy precision measurements [53, 56, 57], with allowed values sensitive to the dark photon mass. The dark photon couples to the SM fermions exclusively via gauge kinetic mixing, except for muons, which also couple through the muon–heavy muon mixing. While the kinetic-mixing portal doesn't play any crucial role, the scalar and Yukawa portals significantly affect Higgs-associated production at a muon collider in this scenario.

The list of free parameters relevant for the discussions in the later sections are mass of the heavy muon (m_{μ_p}), mixing angle between the muon and its heavier counter part ($\sin \theta_L$), mass of the dark photon (m_{γ_d}), the dark gauge coupling (g_d), and the scalar mixing angle ($\sin \theta_s$) along with the SM parameters. Mass of the additional scalar (m_{h_d}) is an independent parameter of the model, however, its impact on our analysis is less significant unlike the scalar mixing angle ($\sin \theta_s$). The kinetic mixing parameter ϵ also does not enter directly in our analysis except the requirement that its value should be small enough to evade the existing constraints and the dark photon decays exclusively to invisible mode via $U(1)_D$ gauge coupling in the range of m_{γ_d} relevant for our analysis.

2.1 Constraints

In this subsection we discuss various observational constraints on the allowed values of the relevant model parameters discussed above.

2.1.1 Constraint on the scalar mixing angle

The scalar mixing angle which simply plays a role of overall coupling rescaling factor in the analysis presented in this paper is constrained by various observations across the mass of the heavy scalar [58–64]. For scalar mass below 100 GeV there are constraints from the LEP experiment and invisible decay of the Higgs boson. For example, if $m_{h_d} < \frac{m_h}{2}$ the corresponding bound on the scalar mixing angle coming from the measurement of the Higgs to invisible final state at LHC is of the order of 0.01 for $v_d \sim 100$ GeV [65, 66]. The LEP experiment suggests $\sin \theta_s$ in the range $(0.9 - 0.998)$ is ruled out for m_{h_d} in the range $10 - 100$ GeV and $v_d \sim v_{EW}$ [58–61, 63]. For masses beyond 100 GeV the constraint coming from collider experiment LHC experiment is more relevant. The constraint on $\sin \theta_s$ in the range $100 \text{ GeV} < m_{h_d} < 200 \text{ GeV}$ is primarily due to the Higgs signal strength measurement and $|\sin \theta_s| > 0.1$ is ruled out in this mass range [63] with $v_d \sim 0.1 \times v_{EW}$. For $m_{h_d} > 200$ GeV, $\sin \theta_s > 0.2$ is disfavored by the LHC data [61, 67].

2.1.2 Lepton flavor universality constraint

In the SM, the universality of the gauge coupling ensures that the Z boson decays in the leptonic final states, in particular, in the final state with electron or muon with equal rate and the ratio of these two rates is predicted to be close to unity in the SM [19]. This has been verified in the LEP experiment at CERN and the observed value of the ratio of these two decay rates (R) is found to be [68]

$$R = \Gamma(Z \rightarrow \mu^+ \mu^-) / \Gamma(Z \rightarrow e^+ e^-) = 1.0009 \pm 0.0028 \quad (16)$$

The model considered in this work introduces a mixing between the second-generation charged lepton and the pVLL. As a consequence, the $Z - \mu - \mu$ vertex, in particular, the $Z - \mu_L^- - \mu_L^-$ interaction vertex is modified to $\frac{g_z}{2}(2 \sin^2 \theta_W - \cos^2 \theta_L)$ (See Eq. (A.7) in Appendix) compared to that³ in the

³The corresponding factor for the SM $Z - \mu_L^- - \mu_L^-$ vertex is $\frac{g_z}{2}(2 \sin^2 \theta_W - 1)$

SM while corresponding right-handed vertex factor remains the same due to the choice of our charge assignment. Therefore, for large mixing one expects deviation in the predicted value of R inconsistent with the above observation. It turns out that, the lepton flavor universality constraint strongly disfavor ($\sin \theta_L > 0.030(0.047)$) at 1σ (2σ) level [27].

2.2 LHC constraints

Various extensions of the SM containing the VLLs have been probed at the LHC as well as at the LEP experiment. Due to the limited center-of-mass energy available at the LEP collider, VLLs with mass above 102.6 GeV [69] are not excluded by the LEP experiment. VLL decaying in the SM mode i.e, νW , ℓZ has been probed at the LHC in the multi-lepton [34, 70] and hadronically decaying tau lepton with additional jets and/or missing transverse energy channels [71, 72]. The ATLAS experiment has searched for VLL mixing with first two generations of charged leptons and has obtained an exclusion limit up to 320 GeV (1220 GeV) on the allowed values of the singlet (doublet) -like electron leptons [34]. The corresponding bound for VLL mixing with muons is 400 GeV (1270 GeV) obtained by same experiment if it is an $SU(2)_L$ singlet (doublet). The CMS experiment at the LHC sets a lower limit on the allowed value of the doublet (singlet) vector-like tau lepton mass to be $\gtrsim 1045$ GeV (150 GeV) with 95 % Confidence Level [70] using 138 fb^{-1} data collected during 2016–2018. The corresponding lower limit obtained by ATLAS experiment on the allowed value of mass of the tau VLL transforming as $SU(2)_L$ doublet is 900 GeV [71]. Moreover, these limits can be relaxed further if the VLLs are allowed to decay in the non-standard modes such as pVLL decaying to a lepton and a dark photon as considered in the present model.

2.3 Electroweak precision constraints

The presence of VLL has various observable consequences and can potentially modify the predictions of the SM. It can contribute to the modification of muon life-time, the branching ratio of $Z \rightarrow \mu^+ \mu^-$, total width of the Z and W bosons and correction to the oblique parameters etc. Since the VLL carries electromagnetic charge it can modify the Higgs to di-photon decay rate as well. In our model, the pVLL can couple to the Higgs via muon-heavy muon mixing and/or Higgs-dark Higgs mixing. Therefore, the corresponding interaction vertices will be proportional to $\sim (y_m \cos \theta_R \cos \theta_L \cos \theta_s + \omega_f \cos \theta_R \sin \theta_L \sin \theta_s)$. Hence, for small $\sin \theta_L$ and $\sin \theta_s$ the deviation from the SM $h - \mu - \mu$ vertex factor is less significant. The correction to the oblique parameters, in particular, S and T due to the singlet VLL is expressed as [73]

$$\Delta T = \frac{m_\mu^2}{16\pi \sin_W^2 m_W^2} \sin^2 \theta_L \left[-(1 + \cos^2 \theta_L) + 2 \cos^2 \theta_L \frac{r_\mu}{r_\mu - 1} \log(r_\mu) + r_\mu \sin^2 \theta_L \right] \quad (17)$$

$$\begin{aligned} \Delta S = & \frac{1}{18\pi} \sin^2 \theta_L \left[\log(r_\mu) + \cos^2 \theta_L \left(\frac{5(r_\mu^2 + 1) - 22r_\mu}{(1 - r_\mu)^2} \right. \right. \\ & \left. \left. + \frac{3(r_\mu + 1)(r_\mu^2 - 4r_\mu + 1)}{(1 - r_\mu)^3} \log(r_\mu) \right) \right] \end{aligned} \quad (18)$$

where, $r_\mu = m_{\mu_p}/m_\mu$.

The updated global fit to the the electroweak precision observables tells that these corrections are constrained as follows [74]:

$$S = -0.05 \pm 0.07 \quad (19)$$

$$T = 0.00 \pm 0.06 \quad (20)$$

In the remaining of this paper, we work with benchmark points consistent with all the constraints mentioned above.

2.4 Muon $g - 2$

The presence of muon–heavy muon–dark photon vertex can give leading contribution to the anomalous muon $g - 2$ at one-loop in this pVLL framework. In the limit $m_{\mu_p} \approx m_{\mu'_p}$ and $m_\mu \approx m_{\mu'} = \frac{1}{\sqrt{2}}y_m v_{\text{EW}}$, this contribution is given by [21, 27]

$$\Delta a_\mu \approx \begin{cases} \frac{g_d^2 m_{\mu'_p} m_\mu}{16\pi^2 m_{\gamma_d}^2} \sin 2\theta_R \sin 2\theta_L, & m_{\mu'_p} \gg m_{\gamma_d} \\ \frac{g_d^2 m_{\mu'_p} m_\mu}{4\pi^2 m_{\gamma_d}^2} \sin 2\theta_R \sin 2\theta_L, & m_\mu \ll m_{\mu'_p} \ll m_{\gamma_d} \end{cases} \quad (21)$$

The current world average value of $\Delta a_\mu = a_\mu^{\text{exp}} - a_\mu^{\text{SM}}$, combining Fermilab Run 1–6 data [75] with the results of Brookhaven experiment [76] is

$$\Delta a_\mu = 38(63) \times 10^{-11} \quad [77] \quad (22)$$

which corresponds to 0.6σ deviation compared to the SM prediction ($a_\mu^{\text{SM}} = 0.00116592033(62)$ [77]).

In Fig. 1, we show the muon $g - 2$ allowed region of parameter space both in the $m_{\gamma_d} - g_d$ and $m_{\mu_p} - m_{\gamma_d}$ planes consistent with Δa_μ mentioned in Eq. (21) at 1σ level. Fig 1a corresponds to $\sin \theta_L = 4 \times 10^{-5}$ and four different heavy muon masses (1 TeV, 1.5 TeV, 2 TeV and 3 TeV), whereas Fig 1b corresponds to two distinct sets of $(g_d, \sin \theta_L)$ with values $(0.05, 4 \times 10^{-5})$ and $(0.5, 1.66 \times 10^{-6})$.

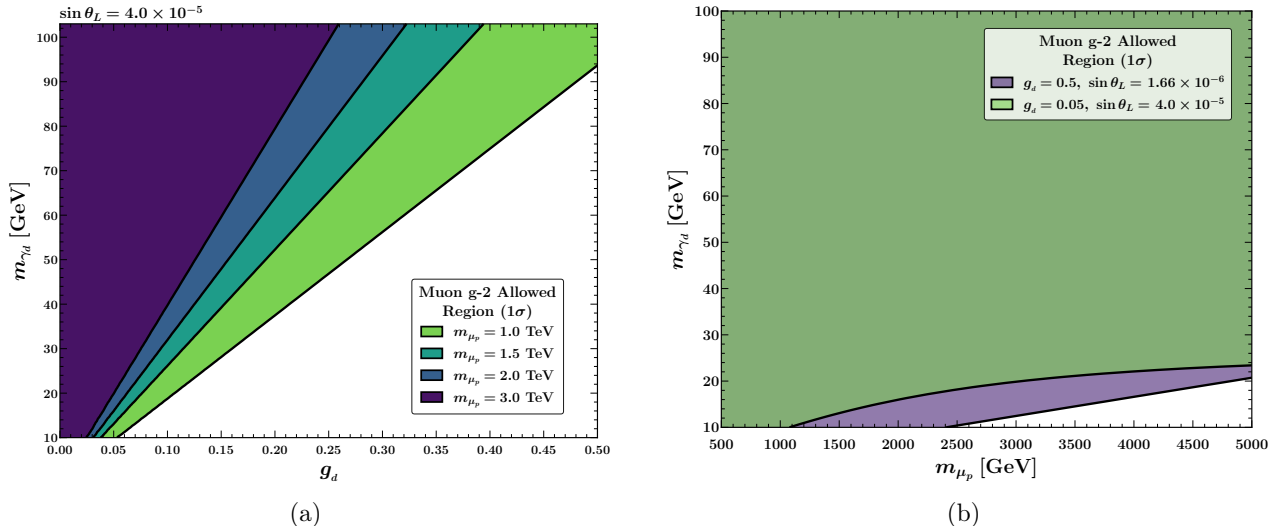


Figure 1: Region (coloured) of parameter space allowed by muon $g - 2$ measurement at 1σ level [77] in the (a) $m_{\gamma_d} - g_d$ plane for $\sin \theta_L = 4 \times 10^{-5}$ and four different m_{μ_p} values (1 TeV, 1.5 TeV, 2 TeV and 3 TeV) and (b) $m_{\mu_p} - m_{\gamma_d}$ plane for two sets of $(g_d, \sin \theta_L)$.

3 Collider Analysis

In this section, we demonstrate the effect of the portal vector-like lepton on the Higgs production in association with a vector boson ($V = Z, \gamma_d$) at future muon collider. We first estimate the effect of pVLL on the production rate of $\mu^+ \mu^- \rightarrow hV$ and compare this w.r.t. the SM prediction of $\mu^+ \mu^- \rightarrow hZ$. The Feynman diagrams for $\mu^+ \mu^- \rightarrow hV$ process are depicted in Fig. 2.

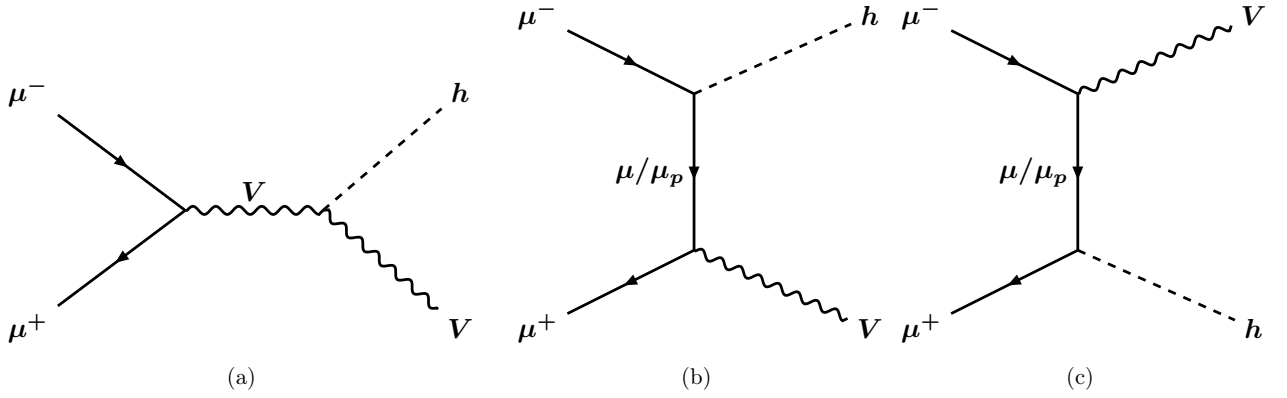


Figure 2: Feynman diagrams for associated production of Higgs and a vector boson ($V = Z, \gamma_d$) at muon collider ($\mu^+ \mu^- \rightarrow hV$).

In order to generate the events and estimate the cross section we first implement the Lagrangian of Eq. (1) in FEYNRULES 2.0 [78]. The Universal FEYNRULES Output [79] of FEYNRULES is then interfaced with event generator MADGRAPH5_AMC@NLO (version 3.5.5) [80] to estimate the leading order (LO) cross section in the context of muon collider.

We have chosen six benchmark points with parameter values consistent with the constraints mentioned in section 2.1, as shown in Table 2.

Benchmark Points	m_{μ_p} [TeV]	$\sin \theta_L$	g_d	$\sin \theta_s$	m_{γ_d} [GeV]
BP1	1	4.0×10^{-5}	0.45	0.05	90
BP2	2	2.0×10^{-5}	0.36	0.05	90
BP3	3	1.7×10^{-6}	0.50	0.05	90
BP4	1	4.0×10^{-5}	0.36	0.05	50
BP5	2	2.0×10^{-5}	0.30	0.05	50
BP6	3	1.7×10^{-6}	0.45	0.05	50

Table 2: Representative benchmark points

3.1 hZ vs $h\gamma_d$ at muon collider

Here we present a comparison between $\mu^+ \mu^- \rightarrow h\gamma_d$ and $\mu^+ \mu^- \rightarrow hZ$ production rates in the context of the model described in section 2 w.r.t. the SM hZ production rate at future muon collider. In Fig. 3, we depict various ratios of cross sections defined in Eq. (23) for three different benchmark points.

$$R_1 = \frac{\sigma_{\text{BSM}}(\mu^+ \mu^- \rightarrow hZ)}{\sigma_{\text{SM}}(\mu^+ \mu^- \rightarrow hZ)} \quad (23a)$$

$$R_2 = \frac{\sigma_{\text{unpol}}(\mu^+ \mu^- \rightarrow h\gamma_d)}{\sigma_{\text{SM}}(\mu^+ \mu^- \rightarrow hZ)} \quad (23b)$$

$$R_3 = \frac{\sigma_{\text{unpol}}^{\text{s-ch}}(\mu^+ \mu^- \rightarrow h\gamma_d)}{\sigma_{\text{SM}}(\mu^+ \mu^- \rightarrow hZ)} \quad (23c)$$

$$R_4 = \frac{\sigma_{\text{unpol}}^{\text{t-ch}}(\mu^+ \mu^- \rightarrow h\gamma_d)}{\sigma_{\text{SM}}(\mu^+ \mu^- \rightarrow hZ)} \quad (23d)$$

$$R_5 = \frac{\sigma_{\text{pol}}^{\text{t-ch}}(\mu_L^+ \mu_R^- \rightarrow h\gamma_d)}{\sigma_{\text{SM}}(\mu^+ \mu^- \rightarrow hZ)} \quad (23e)$$

where,

$$\sigma_{\text{SM}}(\mu^+\mu^- \rightarrow hZ) = \begin{cases} 1.36 \text{ fb}, & \text{for } \sqrt{s} = 3 \text{ TeV} \\ 0.12 \text{ fb}, & \text{for } \sqrt{s} = 10 \text{ TeV} \end{cases} \quad (24)$$

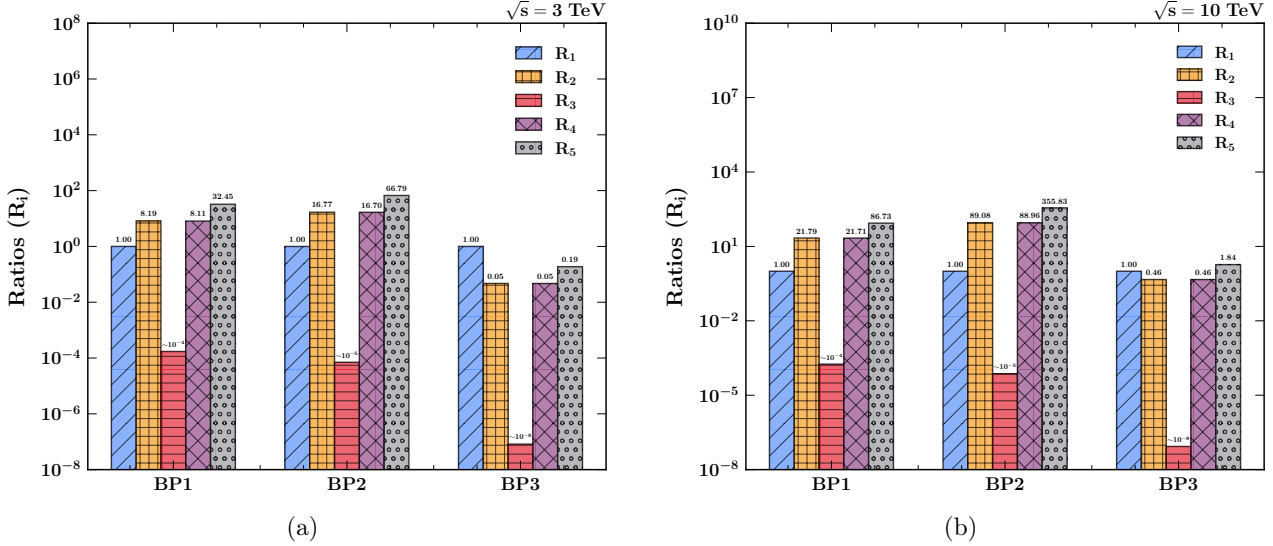


Figure 3: Ratios of cross sections (R_i 's defined in Eq. (23)) for different benchmark points at (a) $\sqrt{s} = 3 \text{ TeV}$ and (b) 10 TeV .

One can see that while the cross section for $\mu^+\mu^- \rightarrow hZ$ production in this scenario remains the same as that in the SM, a higher Higgs production rate is predicted in the $\mu^+\mu^- \rightarrow h\gamma_d$ channel. This is true even for a $\sin \theta_L$ as small⁴ as $\sim 10^{-5}$ with reasonable choices of other relevant parameters (see Table 2 for specification of benchmark points). The underlying reasons behind this is that μ'_R and μ'_{p_R} share identical $SU(2)_L \times U(1)_Y$ charges. Hence, after transforming them into mass eigen-basis using Eq. (10) no off-diagonal $\mu_R^- - \mu_{p_R}^- - Z$ interaction arises. However, the absence of $U(1)_D$ charge for the muon induces an off-diagonal $\mu_R^- - \mu_{p_R}^- - \gamma_d$ interaction in the mass basis. It turns out that the corresponding interaction vertex $\mu_L^+ - \mu_{p_R}^- - Z$ is not present in this model while the $\mu_L^+ - \mu_{p_R}^- - \gamma_d$ (or $\mu_R^- - \mu_{p_L}^+ - \gamma_d$) vertex factor is proportional to $\sim g_d \sin \theta_R \cos \theta_R$ (See Eq. (A.2)). The mixing angle ($\sin \theta_R$) between the right chiral muon and heavy muon is given by

$$\sin \theta_R = \frac{\sin \theta_L}{\sqrt{\frac{m_\mu^2}{m_{\mu_p}^2} \cos^2 \theta_L + \sin^2 \theta_L}} \quad (25)$$

which can reach $\mathcal{O}(0.1)$ value for m_{μ_p} in the TeV range even for a tiny $\sin \theta_L$ ($\sim 10^{-5}$). This is also independently validated by the result that the average unpolarized t/u -channel cross section for $\mu^+\mu^- \rightarrow h\gamma_d$ is dominated by the $\mu_L^+ \mu_R^- \rightarrow h\gamma_d$ contribution and the contribution to the total unpolarized cross section predominantly comes from t/u -channel process compared to pure s -channel contribution. The later is suppressed due to the fact that $\mu_L^+ - \mu_R^- - \gamma_d$ vertex is $\sim g_d \sin^2 \theta_R$.

In Fig. 4 and Fig. 5, we plot R_2 which represents the ratio of average unpolarized cross section for $\mu^+\mu^- \rightarrow h\gamma_d$ to that of SM $\mu^+\mu^- \rightarrow hZ$ (defined in Eq. (23)) in the $m_{\gamma_d} - m_{\mu_p}$ plane at $\sqrt{s} = 3 \text{ TeV}$ and $\sqrt{s} = 10 \text{ TeV}$, respectively, to illustrate the effect of these two parameters on R_2 and hence the $h\gamma_d$ cross section for two different g_d and $\sin \theta_L$ and fixed $\sin \theta_s$. The perturbative unitarity limit obtained using Eq. (15) is also displayed on the same plot. Since the requirement of perturbative unitarity disfavors low values of v_d , one cannot achieve an arbitrary high values of R_2 by going to lower

⁴Small $\sin \theta_L$ ($\sim 10^{-4}$ or less) is favoured by perturbative unitarity requirements for heavy muon mass beyond TeV scale

values of dark photon mass or higher values of g_d and a trade off is maintained in the choice of the two independent parameters m_{γ_d} and g_d .

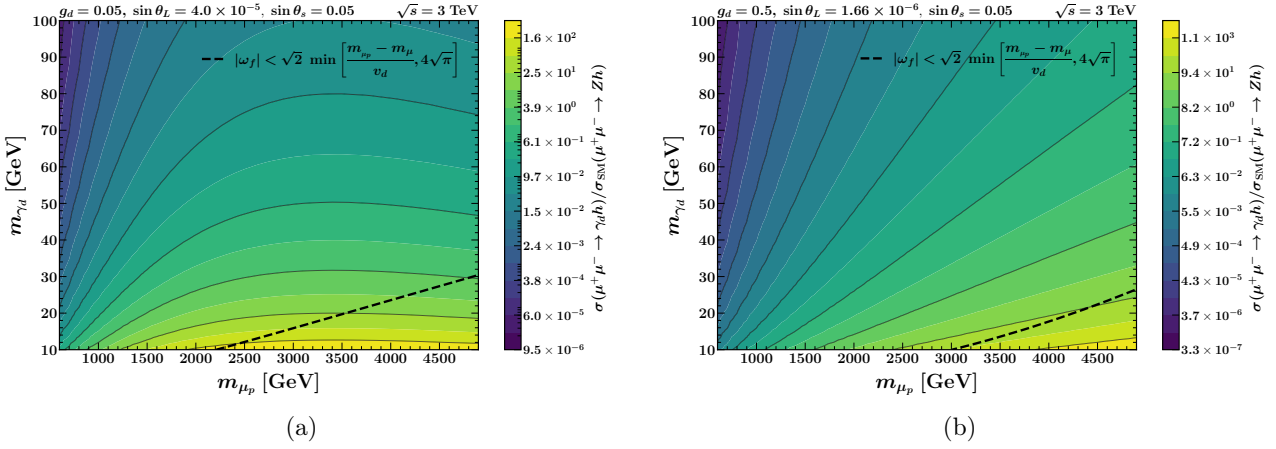


Figure 4: Variation of ratio of cross sections (R_2) for the process $\mu^+ \mu^- \rightarrow h \gamma_d$ with respect to the SM hZ production rate in m_{γ_d} – m_{μ_p} plane assuming $\sqrt{s} = 3$ TeV for two different set of $(g_d, \sin \theta_L)$ and a fixed value of $\sin \theta_s$. (a) The left plot corresponds to $g_d = 0.05$, $\sin \theta_s = 0.05$, and $\sin \theta_L = 4 \times 10^{-5}$ and (b) the right plot corresponds to $g_d = 0.5$, $\sin \theta_s = 0.05$, and $\sin \theta_L = 1.66 \times 10^{-6}$. The region above the dashed (black) line is allowed by the constraint on ω_f described in Eq. (15).

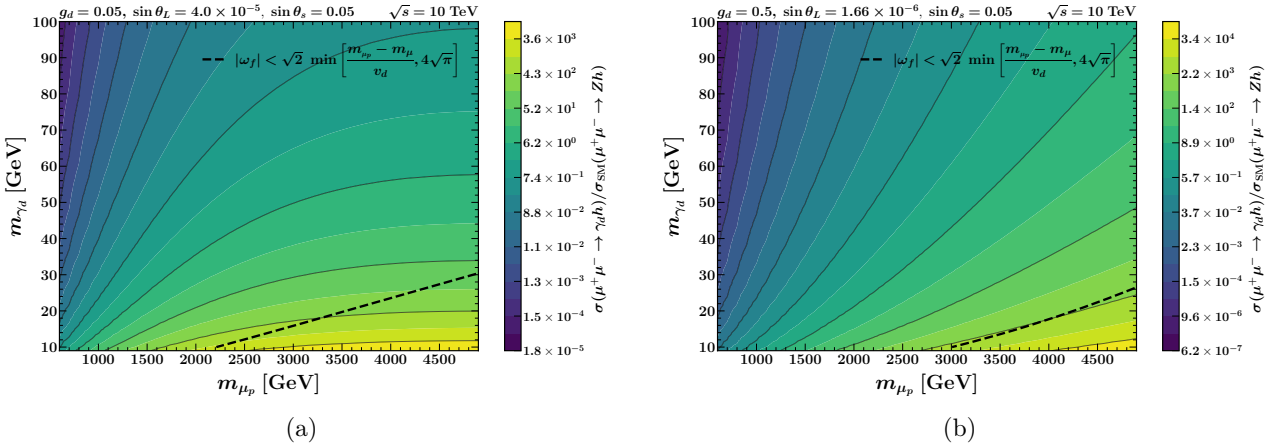


Figure 5: Variation of ratio of cross sections (R_2) for the process $\mu^+ \mu^- \rightarrow h \gamma_d$ with respect to the SM hZ production rate in m_{γ_d} – m_{μ_p} plane assuming $\sqrt{s} = 10$ TeV for two different set of $(g_d, \sin \theta_L)$ and a fixed value of $\sin \theta_s$. (a) The left plot corresponds to $g_d = 0.05$, $\sin \theta_s = 0.05$, and $\sin \theta_L = 4 \times 10^{-5}$ and (b) the right plot corresponds to $g_d = 0.5$, $\sin \theta_s = 0.05$, and $\sin \theta_L = 1.66 \times 10^{-6}$. The region above the dashed (black) line is allowed by the constraint on ω_f described in Eq. (15).

Therefore, depending on the parameter space, Higgs production in association with a dark photon at muon collider can provide us a Higgs production rate higher than hZ production by a factor ranging from 1 to 100.

3.2 Analysis of $h\gamma_d$ process

In the remaining part of this article we focus on the $h\gamma_d$ production at the future muon collider. As discussed above, the rate of this process can be significantly large compared to the hZ production in a wide range of dark photon mass. Hence, it can contribute as an additional channel to the Higgs production at muon collider.

In Fig. 6 we present the LO cross sections for $\mu^+ \mu^- \rightarrow h\gamma_d$ as a function of the center-of-mass energy.

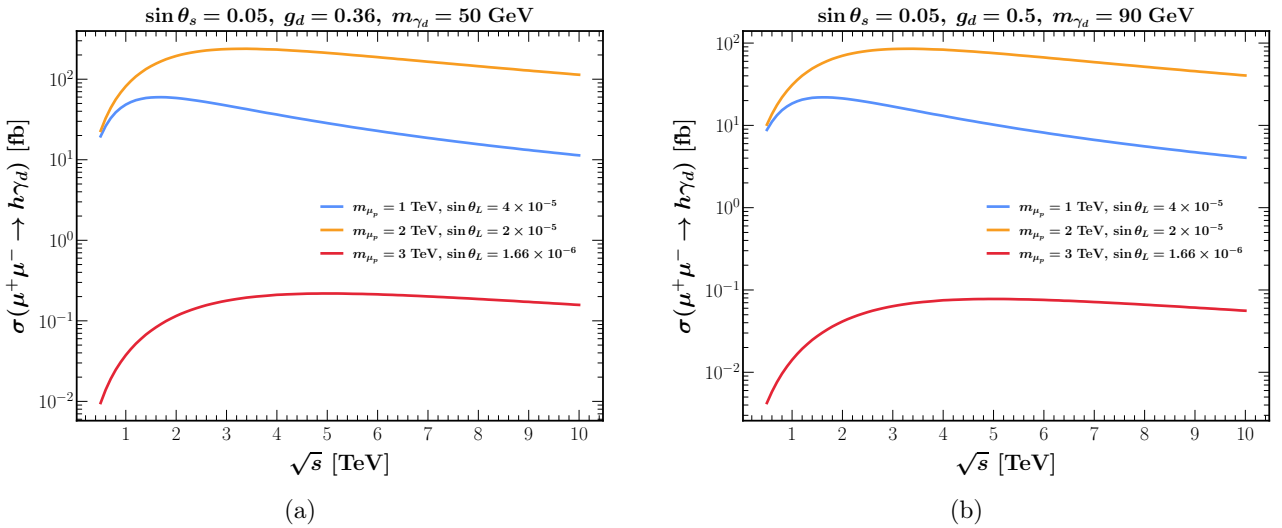


Figure 6: LO cross section for $\mu^+\mu^- \rightarrow h\gamma_d$ as a function of the muon collider center-of-mass energy for various choices of the m_{μ_p} and $\sin\theta_L$ assuming (a) $\sin\theta_s = 0.05$, $g_d = 0.36$, $m_{\gamma_d} = 50$ GeV and (b) $\sin\theta_s = 0.05$, $g_d = 0.50$, $m_{\gamma_d} = 90$ GeV.

The LO cross sections for the process $\mu^+\mu^- \rightarrow h\gamma_d$ for various benchmark points mentioned in Table 2 at the muon collider center-of-mass energies $\sqrt{s} = 3$ TeV and 10 TeV are presented in Table 3.

\sqrt{s} [TeV]	$\sigma(\mu^+\mu^- \rightarrow h\gamma_d)$ [fb]					
	BP1	BP2	BP3	BP4	BP5	BP6
3	11.1	22.8	0.064	47.2	114	0.436
10	2.66	10.9	0.056	11.4	55.0	0.388

Table 3: LO cross sections for $\mu^+\mu^- \rightarrow h\gamma_d$ at $\sqrt{s} = 3$ TeV and 10 TeV for various choices of our benchmark points

The cross section for $h\gamma_d$ production strongly depends on dark photon mass and dark gauge coupling as well as on other model parameters (see Fig. 4, Fig. 5, as well as the corresponding vertex factors in Appendix A and the squared matrix elements in Appendix B). The cross section for the $\mu^+\mu^- \rightarrow h\gamma_d$ process as a function of the dark gauge coupling (g_d) can be parametrized as

$$\sigma_{\text{tot}}(\mu^+\mu^- \rightarrow h\gamma_d) \approx g_d^2 (c_1 \frac{g_d}{m_{\gamma_d}} + c_2)^2 \mathcal{A}_1 + m_{\gamma_d} g_d^3 (c_1 \frac{g_d}{m_{\gamma_d}} + c_2) \mathcal{A}_2 \quad (26)$$

where c_1 , c_2 and \mathcal{A}_1 , \mathcal{A}_2 are in general functions of $(m_{\mu_p}, \sin\theta_L, \sin\theta_s)$ and $(\sqrt{s}, m_{\gamma_d}, m_{\mu_p}, \sin\theta_L, \sin\theta_s)$, respectively. For example, assuming $m_{\gamma_d} = 90$ GeV, $m_{\mu_p} = 1$ TeV, $\sin\theta_L = 4 \times 10^{-5}$ and $\sin\theta_s = 0.05$ one has, at $g_d = 0.45$ and $\sqrt{s} = 3$ TeV

$$c_1 = 16.56 \text{ GeV}, \quad c_2 = 1.72 \times 10^{-8}$$

$$\mathcal{A}_1 = 7.96 \times 10^3 \text{ fb}, \quad \mathcal{A}_2 = 0.145 \text{ fb GeV}^{-1}$$

While writing down the above parametric equation a particular helicity configuration of the initial state muons have been considered that gives dominant contribution to the total unpolarized cross section as explained earlier. Also we have ignored the pure s -channel and any t/u -channel muon mediated contributions. In Eq. (26), the first term corresponds to pure t/u -channel heavy muon mediated contribution while the second term represents its interference with the s -channel diagram.

The dark photon in this scenario is considered to be *invisible* and hence gives rise to missing energy signature at the muon collider. The Higgs on the other hand predominantly decays to a pair of bottom quarks. Therefore, the final state consists of $b\bar{b}$ *along with missing energy* at muon collider (see Fig. 7).

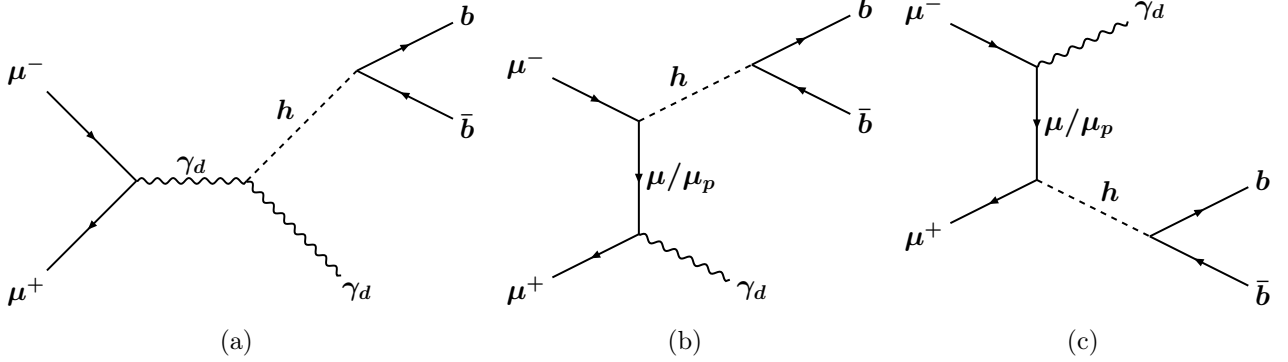


Figure 7: Feynman diagrams for the subprocess, $\mu^+\mu^- \rightarrow h(b\bar{b}) + \gamma_d$ leading to $b\bar{b}$ *plus missing energy* final state.

The dominant SM backgrounds that contribute to the $b\bar{b}$ *plus missing energy* final state, namely, $\mu^+\mu^- \rightarrow b\bar{b}\nu\bar{\nu}$ process comes from hZ , ZZ , $h\nu\bar{\nu}$, $Z\nu\bar{\nu}$ and non-resonant $b\bar{b}\nu\bar{\nu}$ productions at muon collider. They can be sub-divided into $2 \rightarrow 2$, $2 \rightarrow 3$ and $2 \rightarrow 4$ categories as follows

- (a) $\mu^+\mu^- \rightarrow hZ \rightarrow (b\bar{b})(\nu\bar{\nu})$,
- (b) $\mu^+\mu^- \rightarrow ZZ \rightarrow (b\bar{b})(\nu\bar{\nu})$,
- (c) $\mu^+\mu^- \rightarrow h\nu\bar{\nu} \rightarrow (b\bar{b})\nu\bar{\nu}$,
- (d) $\mu^+\mu^- \rightarrow Z\nu\bar{\nu} \rightarrow (b\bar{b})\nu\bar{\nu}$,
- (e) $\mu^+\mu^- \rightarrow b\bar{b}\nu\bar{\nu}$ (non-resonant).

Some representative Feynman diagrams corresponding to these SM background subprocesses are shown in Fig. 8.

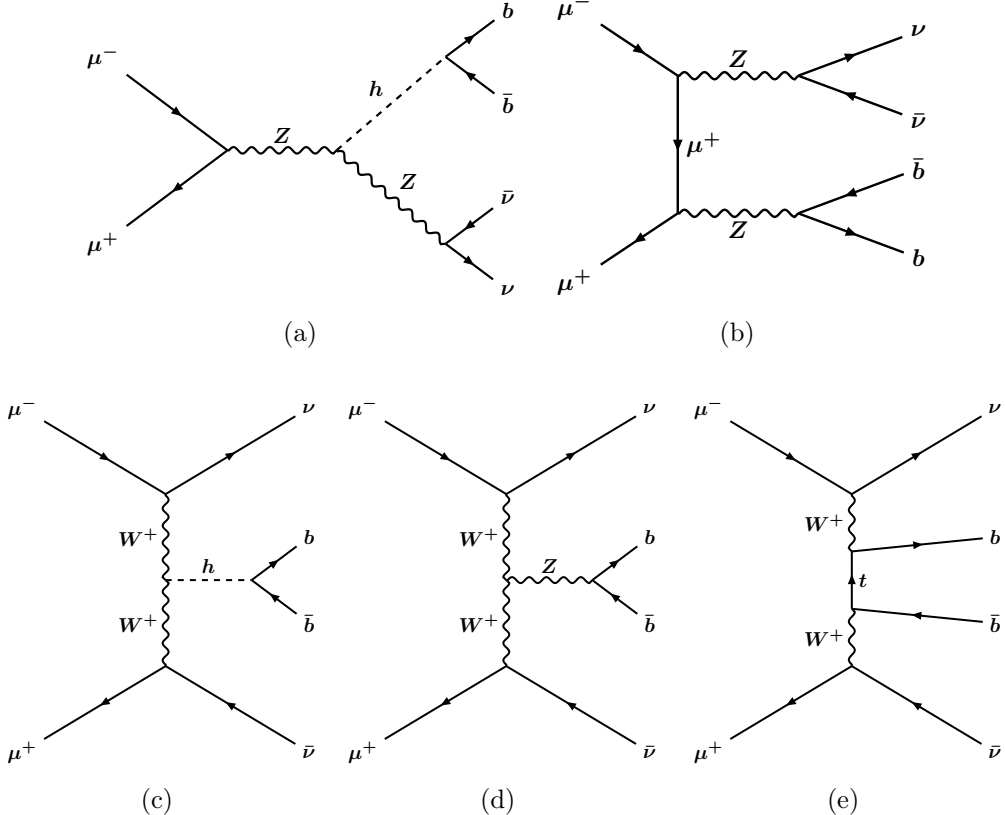


Figure 8: Feynman diagrams for various SM background subprocesses leading to $b\bar{b}\nu\bar{\nu}$ final state in $\mu^+\mu^-$ collisions.

In Table 4, we tabulate the cross sections for the aforementioned SM background subprocesses at 3 and 10 TeV $\mu^+\mu^-$ collision energies. It is obvious that the dominant contribution to the total SM background comes from the resonant $b\bar{b}$ production.

Background processes	σ [fb] at $\sqrt{s} = 3$ TeV	σ [fb] at $\sqrt{s} = 10$ TeV
$\mu^+\mu^- \rightarrow hZ \rightarrow (b\bar{b})(\nu\bar{\nu})$	0.18	0.02
$\mu^+\mu^- \rightarrow ZZ \rightarrow (b\bar{b})(\nu\bar{\nu})$	1.45	0.18
$\mu^+\mu^- \rightarrow h\nu\bar{\nu} \rightarrow (b\bar{b})\nu\bar{\nu}$	318	540
$\mu^+\mu^- \rightarrow Z\nu\bar{\nu} \rightarrow (b\bar{b})\nu\bar{\nu}$ ⁵	305	526
$\mu^+\mu^- \rightarrow b\bar{b}\nu\bar{\nu}$ (total)	641	1101

Table 4: LO cross sections (in fb) for various SM background subprocesses contributing to the $b\bar{b}\nu\bar{\nu}$ final state in $\mu^+\mu^-$ collision at $\sqrt{s} = 3$ TeV and 10 TeV. The values in the last row (**boldface**) take into account contributions from all possible subprocesses leading to $b\bar{b}\nu\bar{\nu}$ final state including those mentioned in the table.

Events generated using the event generator `MADGRAPH5_AMC@NLO` for both the signal and the SM background processes are then interfaced with `PYTHIA8` (version 8.3) [81] for showering, hadronization, decay and further collider analysis. The detector response in the context of future muon collider is parametrized using a Gaussian smearing function as given in Eq. (27) following the Ref. [82, 83].

$$\frac{\sigma_E}{E} = \sqrt{\left(\frac{N}{E}\right)^2 + \left(\frac{S}{\sqrt{E}}\right)^2 + C^2} \quad (27)$$

where E is the energy associated with the final state object and σ_E is the standard deviation in the measurement of E . The parameters N , S and C represents respectively the noise, stochastic and the constant terms. Depending on the detector these parameters have different values for specific final state objects. In the context of future muon collider for jets in the central region ($|\eta| < 2.5$), we have used the following set of values for these parameters [84]

$$N = 0, \quad S = 0.3, \quad C = 0.05$$

In Fig. 9, we plot the central-jet⁶ number distributions for various signal benchmark points. We have used anti-kt jet clustering algorithm [85] with clustering radius $R=0.4$ using `FastJet` (version 3.5.0) [86]. This has been done keeping in mind the fact that at the muon collider center-of-mass energies ($\sqrt{s} = 3$ TeV and 10 TeV), both the Higgs and the dark photon are always highly boosted, each sharing almost half of the available center-of-mass energies. Therefore, most of the signal events are expected to have one collimated $b\bar{b}$ pair originating from the Higgs decays resulting into a single narrow jet. Only a fraction of signal events due to final state radiation, showering and hadronization effect result into events with more than one central-jet.

It turns out at 3 TeV center-of-mass energy ($\sim 87-90\%$) of the signal events consists of *exactly one central-jet* and remaining $10-13\%$ corresponds to *exactly two central-jet* events. This pattern changes at 10 TeV center-of-mass energy. In this case, almost all the signal events ($\gtrsim 96\%$) correspond to one central-jet, as expected. The central-jet number distribution corresponding to the total SM background in the $b\bar{b}\nu\bar{\nu}$ final state is also displayed on the same figure. One can see that the SM background events are distributed among 0, 1, 2 or 3 central-jet events categories. At $\sqrt{s} = 3$ TeV the distribution has a peak around $N_{\text{c-jet}} = 2$ containing almost 54% of the total background events. At 10 TeV center-of-mass energy, there is a significant decrease (increase) in number of events in exactly two (zero) central-jet event categories.

⁶Jets with transverse momentum $p_T > 20$ GeV and pseudo-rapidity $|\eta| < 2.5$

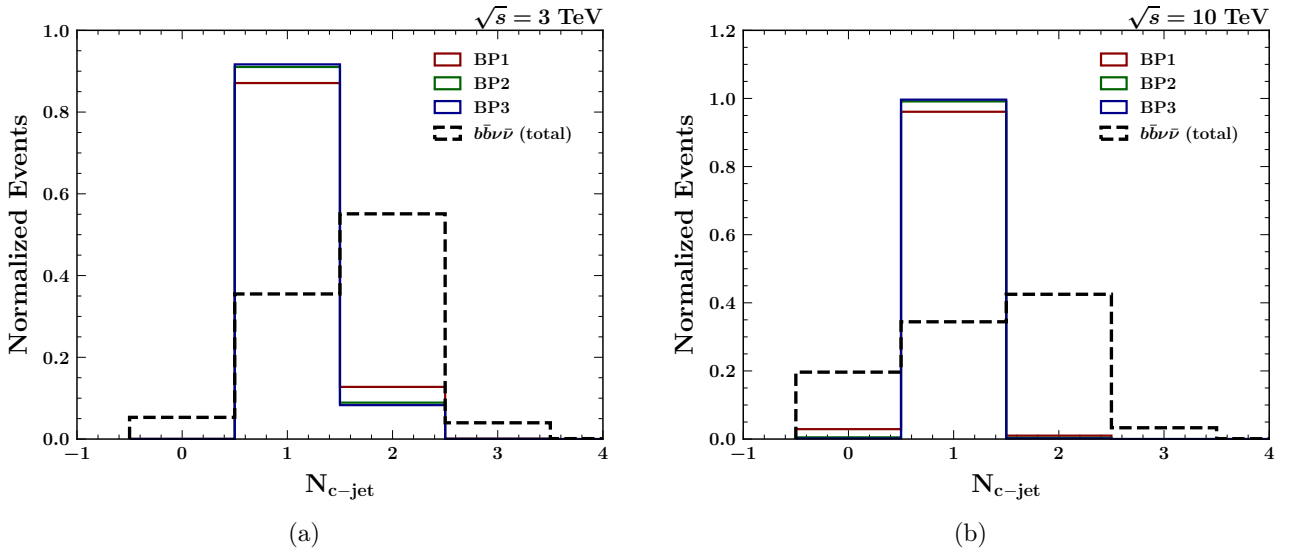


Figure 9: Central-jet ($N_{c\text{-jet}}$) multiplicity distribution at $\sqrt{s} = 3$ TeV and 10 TeV for three different signal benchmark points and the total SM background.

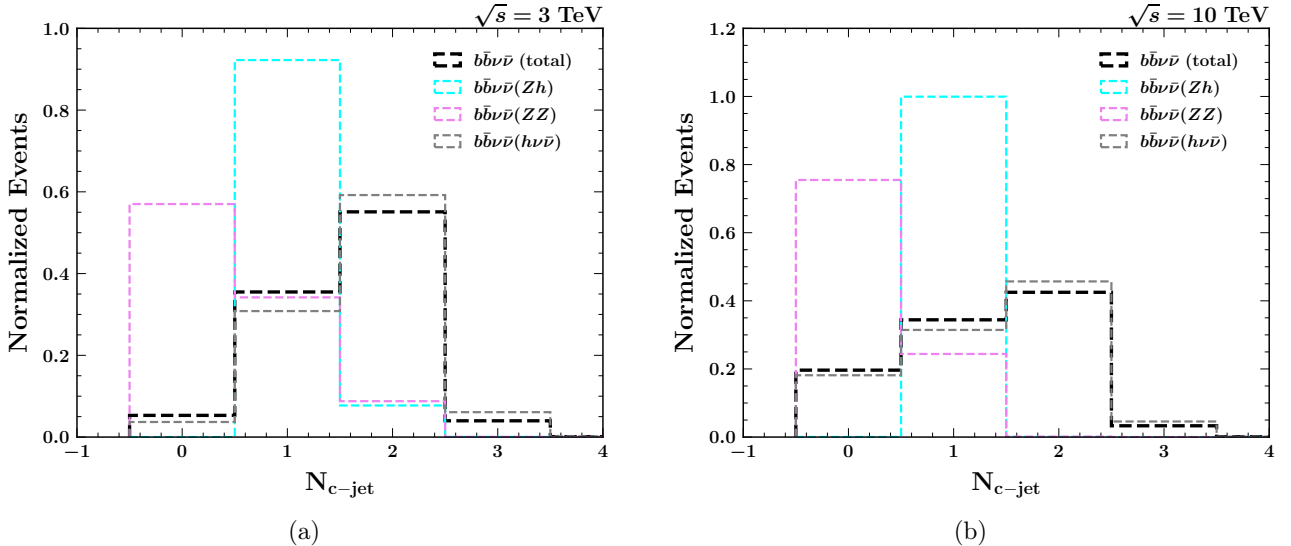


Figure 10: Central-jet ($N_{c\text{-jet}}$) multiplicity distribution at $\sqrt{s} = 3$ TeV and 10 TeV for various SM background subprocesses and the total background.

This behavior arises because a significant fraction of the background originates from $2 \rightarrow 3$ processes such as $h\nu\bar{\nu}$ and $Z\nu\bar{\nu}$ ⁷. In these cases, the Higgs or Z boson produced in association with a neutrino pair is generally not boosted, often resulting in multi-jet final states. Similar arguments apply to the continuum $b\bar{b}\nu\bar{\nu}$ background. In contrast, the SM hZ and ZZ backgrounds, although both are $2 \rightarrow 2$ processes, display different central-jet number distributions. This distinction arises because the hZ is predominantly an s -channel process, whereas the ZZ process proceeds via t/u -channel muon mediation, leading to different angular distributions of the final-state particles. Consequently, the ZZ process is expected to give more zero central-jet events than hZ . This feature is also reflected in Fig. 10.

This motivates us to focus on two different final states, namely, *leptonically quiet exactly one central-jet and exactly two central-jets, both in conjunction with missing energy* at two different $\mu^+\mu^-$ collision energies ($\sqrt{s} = 3$ TeV and 10 TeV).

⁷We have not explicitly shown corresponding distributions for $Z\nu\bar{\nu}$ and also in the context of distributions of various kinematical variables later on as it will also contain the contributions coming from $\mu^+\mu^- \rightarrow ZZ$ process.

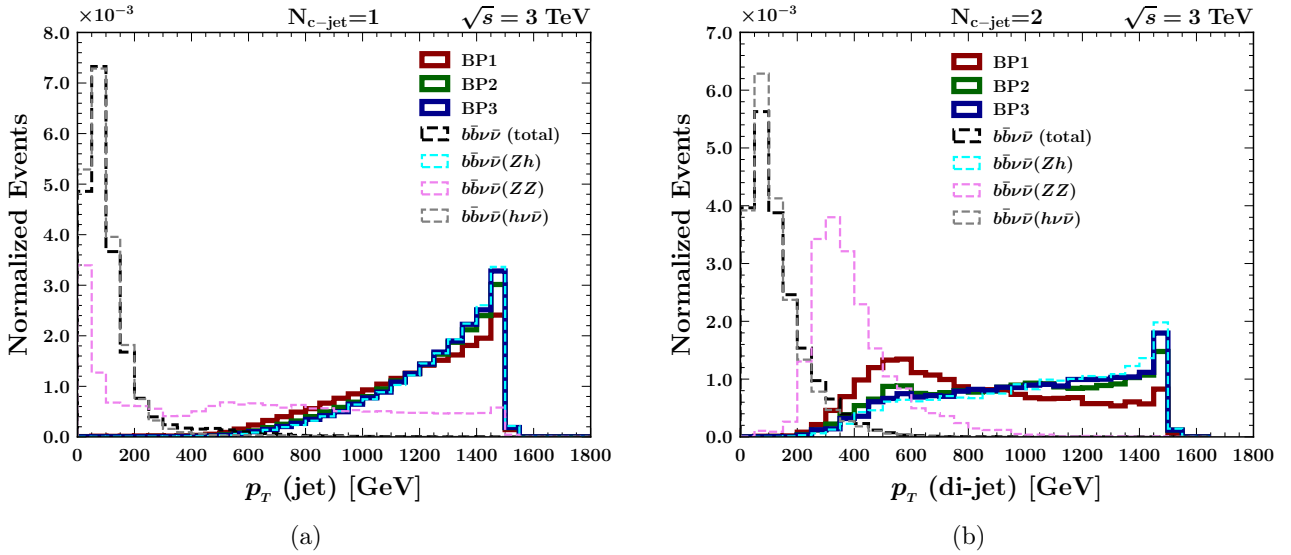


Figure 11: Transverse momentum (p_T) distributions of the (a) jet and (b) the di-jet in the $N_{c\text{-jet}} = 1$ and $N_{c\text{-jet}} = 2$ final states, respectively, at 3 TeV muon collider center-of-mass energy for both signal and the SM background events.

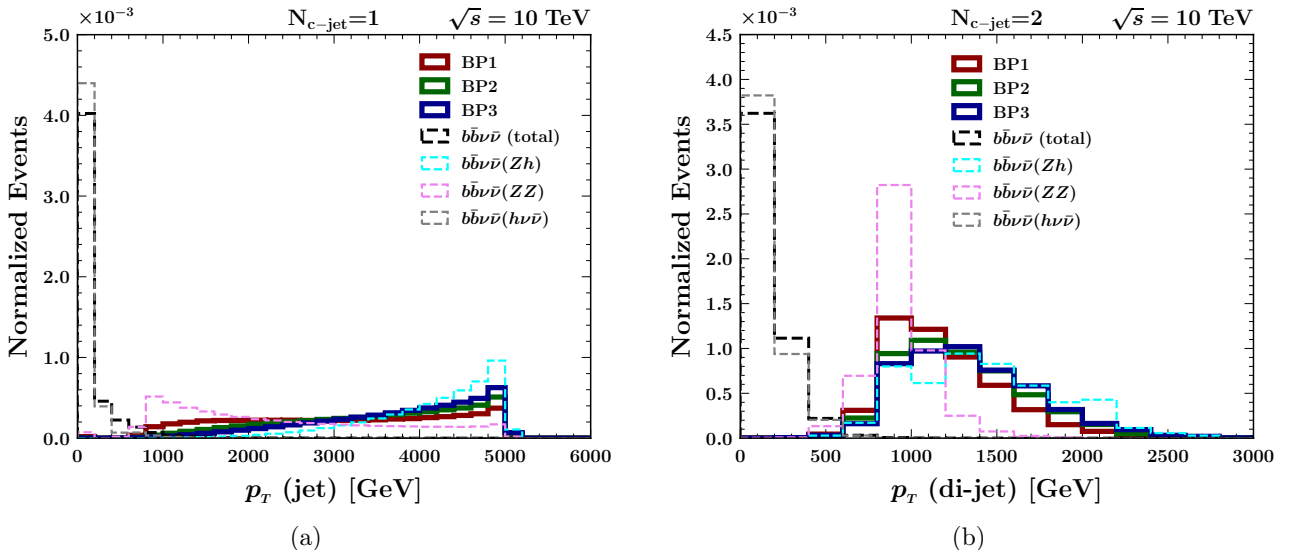


Figure 12: Transverse momentum (p_T) distributions of the (a) jet and (b) the di-jet in the $N_{c\text{-jet}} = 1$ and $N_{c\text{-jet}} = 2$ final states, respectively, at 10 TeV muon collider center-of-mass energy for both signal and the SM background events.

As already mentioned, Higgs boson produced at the future muon collider center-of-mass energies in a $2 \rightarrow 2$ process are typically highly boosted. The Higgs subsequently decays into a pair of bottom quarks which due to their small angular separation, manifest as a single collimated jet in the detector. In Fig. 11 and 12, we plot the transverse momentum distributions of a jet or di-jet system, as applicable, for two different muon collider center-of-mass energies. The purpose of these distributions are two-fold. They provide an explanation of Fig. 9 and 10 and also give a motivation for the following discussion.

To identify and analyze the boosted Higgs jets, we employ jet substructure analysis and dedicated Higgs tagging techniques. For this purpose we have used *MassDropTagger* [87] to identify a boosted Higgs structure inside jets. These jets are obtained after re-clustering all the hadrons in a particular final state with Cambridge-Aachen (CA) jet clustering algorithm [88] and energy-scheme recombination assuming jet-clustering radius⁸ $R = 1.2$. The CA algorithm is chosen because it clusters particles based

⁸We call these jets as CA_{1.2} jets. Also the above analysis is not too sensitive to the choice of the jet clustering radius values. The algorithm works fine in the range $0.8 \leq R \leq 1.4$.

solely on angular distance, making it well-suited for subsequent substructure analyses.

Below we briefly summarize the algorithm behind the jet substructure analysis implemented in *MassDrop Tagger*:

1. The leading- p_T jet (with transverse momentum $p_T > 200$ GeV) is first passed through the *MassDrop Tagger* procedure. The algorithm iteratively de-clusters the jet to find an imprint of a heavy-particle by applying the following two conditions characterized by the dimensionless parameters μ and y_{cut} :

$$\begin{aligned} \text{i) Mass-drop condition : } & \frac{m_{j_1}}{m_j} < \mu \\ \text{ii) Symmetry condition: } & y = \frac{\min(p_{Tj_1}^2, p_{Tj_2}^2)}{m_j^2} \Delta R_{j_1 j_2}^2 > y_{\text{cut}}. \end{aligned}$$

where j_1 and j_2 (with $m_{j_1} > m_{j_2}$) denote the two sub-jets obtained by undoing the final stage of clustering of a parent jet j . Here, $\Delta R_{j_1 j_2}$ (with $\Delta R = \sqrt{\Delta\eta^2 + \Delta\phi^2}$) is the angular separation between the two sub-jets in the $\eta - \phi$ plane. The values of the dimensionless parameters μ and the y_{cut} are 0.67 and 0.09, respectively [87].

2. If both the above criteria are satisfied, the jet is tagged as a boosted heavy-particle candidate consisting of two sub-jets j_1 and j_2 . Otherwise, the lighter sub-jet is discarded, and the procedure is repeated by treating j_1 as the parent jet until a valid substructure is identified. We select an event for further analysis if it contains at least one CA_{1.2} jet with a substructure.

As discussed earlier in this section, the dominant contribution to the total SM background cross section (approximately 0.641 pb at $\sqrt{s} = 3$ TeV) arises from $2 \rightarrow 3$ processes such as $\mu^+ \mu^- \rightarrow h \nu \bar{\nu}$ and $\mu^+ \mu^- \rightarrow Z \nu \bar{\nu}$. The application of jet-substructure techniques or the use of the transverse momentum of the $b\bar{b}$ system, in combination with missing energy, proves highly effective in suppressing these dominant SM background components. Consequently, only the $2 \rightarrow 2$ processes like $\mu^+ \mu^- \rightarrow ZZ$ and $\mu^+ \mu^- \rightarrow hZ$ surpass the substructure requirement. However, the cross sections for these later processes are significantly smaller compared to the total SM background cross section (see Table 4).

3.3 Kinematic variables

In this subsection we discuss few useful kinematic variables and choice of selection cuts. The next stage of our cut based analysis utilizes both the missing energy and invariant mass of a jet (or di-jet system) to reduce/eliminate the SM backgrounds.

- **Missing energy (\cancel{E}):** In collider experiments, missing energy corresponds to the total energy carried by the invisible particles which remain unobserved at the detector level. In a particular final state consisting of both visible and invisible particles, using the energy conservation we can find the missing energy of the system as

$$\cancel{E} = \sqrt{s} - E_{\text{vis}} \quad (28)$$

where, \sqrt{s} is center-of-mass energy of the collisions and E_{vis} is the total energy of all the visible final state particles.

In collider investigations, the visible particles in general consist of the hadrons clustered as jets, isolated photons and leptons, and soft unclustered components. Thus, the expression of missing energy at the detector level can be written as

$$\cancel{E} = \sqrt{s} - \left(\sum_{i \in \text{iso leps}} E(i) + \sum_{i \in \text{iso phos}} E(i) + \sum_{i \in \text{jets}} E(i) + \sum_{i \in \text{soft}} E(i) \right) \quad (29)$$

In Fig. 13, we plot the missing energy distributions for the signal events for various benchmark scenarios corresponding to two different final states at center-of-mass energy $\sqrt{s} = 3$ TeV. The

corresponding distributions at 10 TeV center-of-mass energy are shown in Fig. 14. The contribution to the missing energy for the signal events is due to the invisible dark photon and the distribution is expected to peak $\sim \sqrt{s}/2$ (neglecting the finite mass effect) in a $2 \rightarrow 2$ process. However, due to the presence of additional neutrinos coming from B meson decays the missing energy distribution extends beyond $\sqrt{s}/2$. The SM background events in the $b\bar{b}\nu\bar{\nu}$ final state has dominant contribution from the $2 \rightarrow 3$ processes such as $h\nu\bar{\nu}$ and $Z\nu\bar{\nu}$. Together they form the 99 % of the total cross section and only a very small fraction of it comes from $2 \rightarrow 2$ processes like ZZ and hZ . The pair of neutrinos in the $h\nu\bar{\nu}$ or $Z\nu\bar{\nu}$ processes carries maximum share of the available center-of-mass energy. Hence, the missing energy distribution for the SM background events has a peak mostly around \sqrt{s} . This is reflected in the missing energy distributions for individual SM background components and the total SM background as depicted in the same figures. Therefore, missing energy variable is an extremely useful discriminator between the signal and the background.

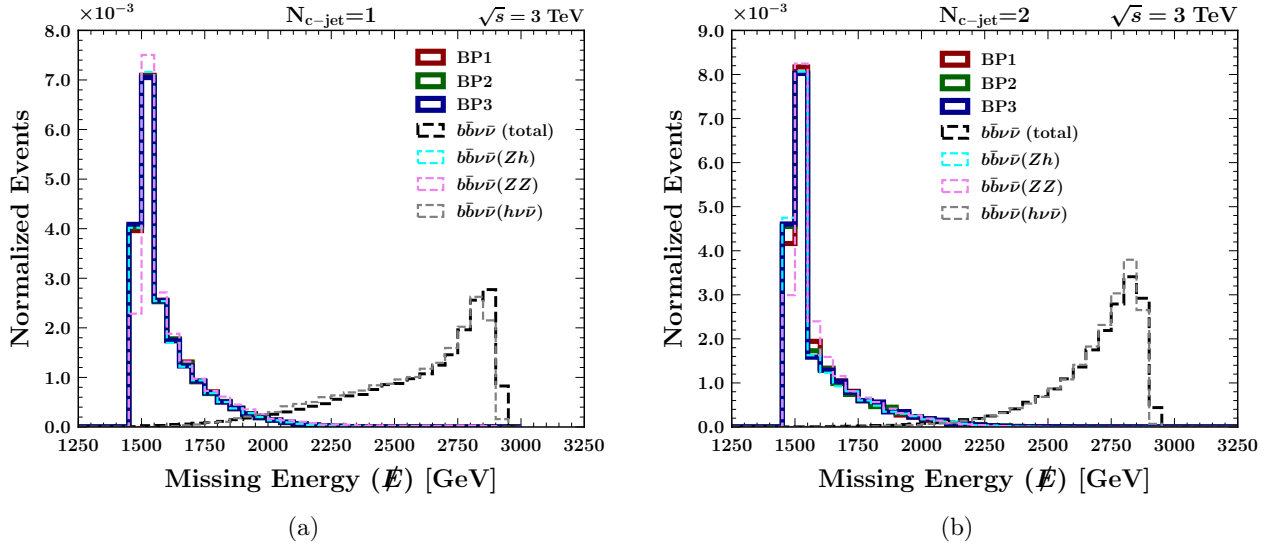


Figure 13: Missing energy (\cancel{E}) distributions at $\sqrt{s} = 3$ TeV in the (a) $N_{c\text{-jet}} = 1$ and (b) $N_{c\text{-jet}} = 2$ final states for both signal and SM background events.

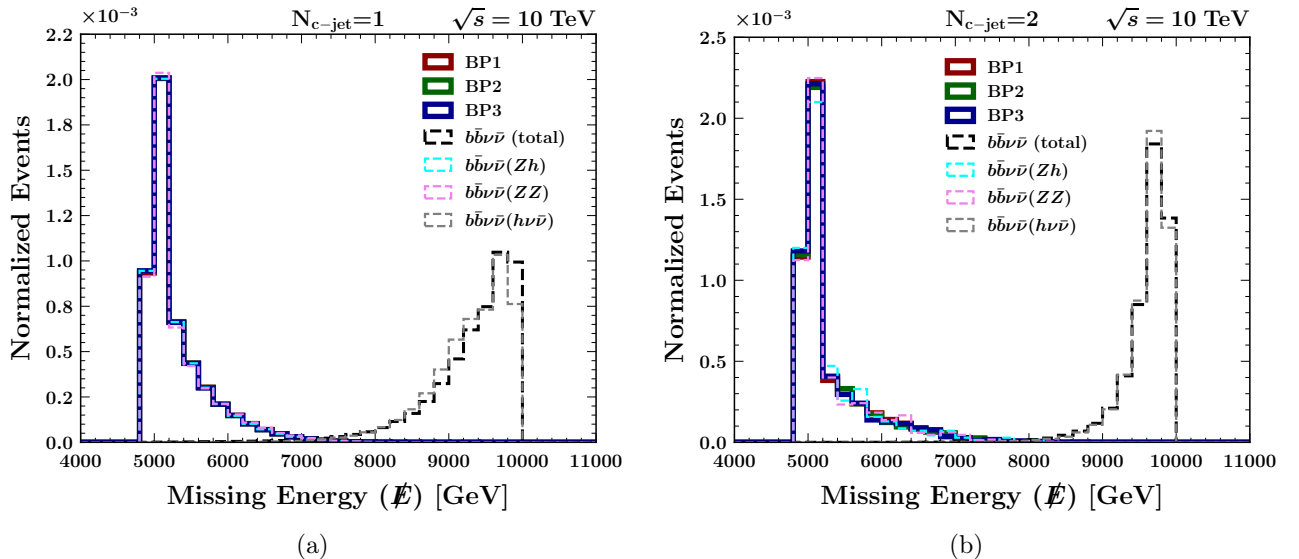


Figure 14: Missing energy (\cancel{E}) distributions at $\sqrt{s} = 10$ TeV in the (a) $N_{c\text{-jet}} = 1$ and (b) $N_{c\text{-jet}} = 2$ final states for both signal and SM background events.

- **$b\bar{b}$ invariant mass ($M_{b\bar{b}}$)** : In our analysis the invariant mass associated with the $b\bar{b}$ system is

extracted in two different ways using the following formula

$$M_{12}^2 = (p_1 + p_2)^2 = (E_1 + E_2)^2 - |\vec{p}_1 + \vec{p}_2|^2 \quad (30)$$

where $p_1 = (E_1, |\vec{p}_1|)$ and $p_2 = (E_2, |\vec{p}_2|)$ are the four momentum associated with the two sub-jets (jets) in the final state comprising one (two) central-jet. In events with *exactly one central-jet* we combine the four momentum of the two sub-jets inside a boosted CA_{1.2} jet to get the invariant mass distribution. Whereas in the $N_{c\text{-jet}} = 2$, case we combine the four momentum of two AK4 jets in order to get the invariant mass associated with the di-jet system. The corresponding distributions in these two final states are plotted in Fig. 15 and 16. One can see that for signal events this distribution has a peak near the Higgs mass. Whereas the same for the background components peak at varying locations, namely, at the mass of the Higgs and Z boson as expected. One also sees a peak at a very low invariant mass which has origin in the final state radiation and hadronization effect from one of the bottom quarks only, and may give rise to jet substructure. In events with *two central-jets* in final state one has two clear peaks at the values of Z and Higgs mass in the invariant mass distribution corresponding to the background subprocesses. This is due to the presence of ZZ , $Z\nu\bar{\nu}$ component as well as hZ and $h\nu\bar{\nu}$ components of the total SM background. The tail in all these invariant mass distributions at values lower than the peak values is due to the missing momentum component associated with the invisible neutrinos produced in B decays.

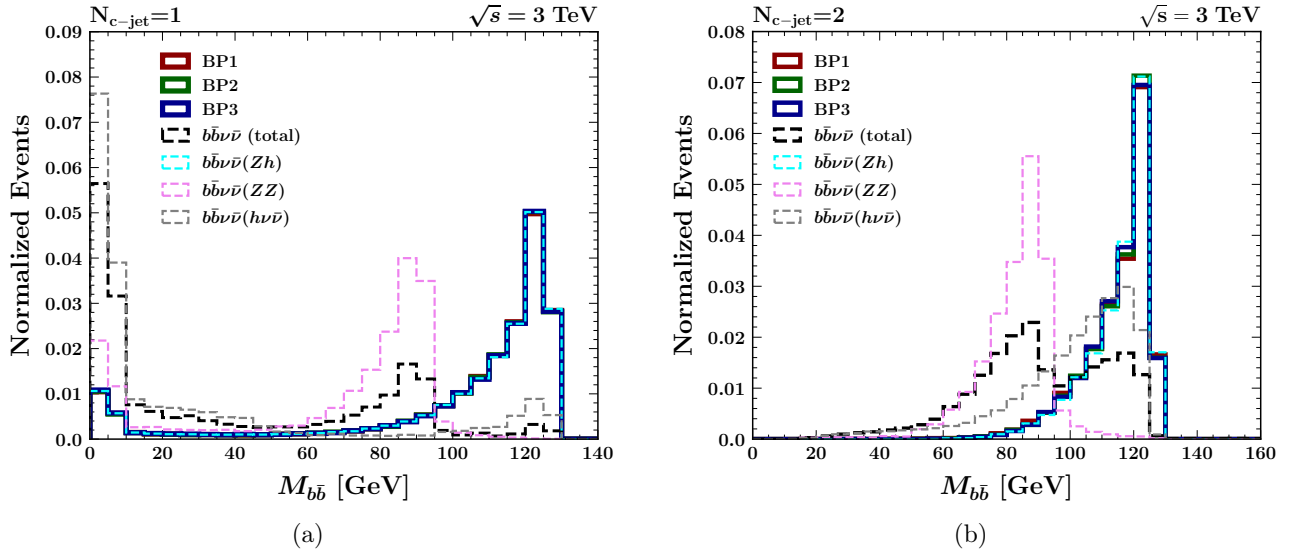


Figure 15: Invariant mass (M_{bb}) distribution at $\sqrt{s} = 3$ TeV in the (a) $N_{c\text{-jet}} = 1$ and (b) $N_{c\text{-jet}} = 2$ final state for both signal and background events.

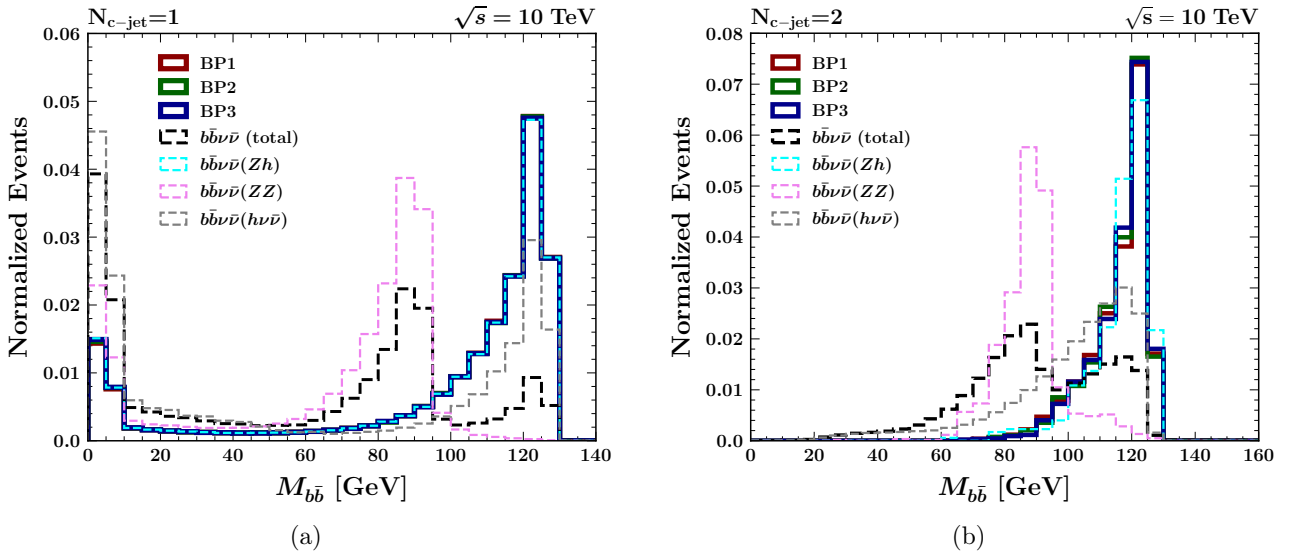


Figure 16: Invariant mass ($M_{b\bar{b}}$) distribution at $\sqrt{s} = 10$ TeV in the (a) $N_{c\text{-jet}} = 1$ and (b) $N_{c\text{-jet}} = 2$ final state for both signal and background events.

One can see that the *normalized* signal distributions are mostly insensitive to the intermediate heavy muon mass. While presenting the kinematic distributions for the signal benchmark points (BPs) we have chosen (BP1, BP2 and BP3) as our representative BPs corresponding to three different heavy muon masses (1, 2 and 3 TeV). Similar distributions exist for other signal benchmark points {BP4–BP6} corresponding to $m_{\gamma_d} = 50$ GeV as well. However, the effect of the dark photon mass on the normalized distributions are not significant enough. Hence, we choose not to display them here as they closely resemble the distributions already presented.

3.4 Cuts

To separate the signal from the corresponding SM background, we have used the following selection cuts on the observables associated with the individual final states.

- $\cancel{E} < \cancel{E}_0$, where $\cancel{E}_0 = 2$ (7) TeV for $\sqrt{s} = 3$ (10) TeV.
- Jet substructure requirement
- $M_{b\bar{b}} > M_0$, where $M_0 = 95$ GeV.

4 Results

In this section, we present the results of our analysis of the process Higgs production in association with a dark photon at the future muon collider. In the previous section, we have discussed the production rate of $\mu^+\mu^- \rightarrow h\gamma_d$ and its comparison with the SM hZ production in presence of the portal vector-like lepton. It also includes the choice of various kinematic variables and selection criteria. In Table 5 and 7, we tabulate the production cross sections for the signal process as well as the effects of our selection criteria on it for various choices of our benchmark points (BP1-BP6) in the *exactly one and two central-jet(s)* final states at $\sqrt{s} = 3$ TeV and 10 TeV, respectively. The signal cross sections mentioned in these tables assume $h \rightarrow b\bar{b}$ decay branching ratio (BR) to be 100%. The effect of cut-flow on the individual SM background components (hZ , ZZ , $h\nu\bar{\nu}$) and the total SM background contribution in the $b\bar{b}\nu\bar{\nu}$ final state are presented in Table 6 and Table 8 at muon collider center-of-mass energies 3 and 10 TeV, respectively. These cross sections are quoted taking into account appropriate decay BRs, as applicable. Since $\mu^+\mu^- \rightarrow h\nu\bar{\nu}/Z\nu\bar{\nu}$ form the dominant component of the total SM background, a significant reduction of the total background rate after rejecting events beyond a certain missing energy value (\cancel{E}_0) is due to the fact that corresponding $h\nu\bar{\nu}$ and $Z\nu\bar{\nu}$ contributions become significantly small in this phase space region. This is also visible in Fig. 13 and 14.

BPs	Production cross-section (fb)	Cross sections (fb): $N_{c\text{-jet}} = 1$ final state				Cross sections (fb): $N_{c\text{-jet}} = 2$ final state					
		Basic Cuts	\cancel{E} cut ($\cancel{E} < \cancel{E}_0$)	Jet substructure requirement	$M_{b\bar{b}}$ cut ($M_{b\bar{b}} > M_0$)	Basic Cuts	\cancel{E} cut ($\cancel{E} < \cancel{E}_0$)	Jet substructure requirement	$M_{b\bar{b}}$ cut ($M_{b\bar{b}} > M_0$)		
		BP1	11.1	9.70	9.51	9.39	7.36	1.42	1.38	1.30	1.24
BP2	22.8		20.7	20.3		20.1	15.7	2.03	1.97	1.84	1.76
BP3	0.064		0.059	0.058		0.057	0.044	0.005	0.005	0.005	0.005
BP4	47.2		41.1	40.3		39.8	31.3	5.97	5.79	5.49	5.24
BP5	114		104	102		101	78.8	9.95	9.63	8.97	8.65
BP6	0.436		0.401	0.393		0.388	0.303	0.035	0.034	0.031	0.030

Table 5: The effect of cut-flow on the signal cross section for various representative benchmark points in two different final states ($N_{c\text{-jet}} = 1$ and $N_{c\text{-jet}} = 2$) at $\sqrt{s} = 3$ TeV assuming $\text{BR}(h \rightarrow b\bar{b}) = 1$.

Background processes	Production cross-section (fb)	Cross sections (fb): $N_{c\text{-jet}} = 1$ final state				Cross sections (fb): $N_{c\text{-jet}} = 2$ final state					
		Basic Cuts	\cancel{E} cut ($\cancel{E} < \cancel{E}_0$)	Jet substructure requirement	$M_{b\bar{b}}$ cut ($M_{b\bar{b}} > M_0$)	Basic Cuts	\cancel{E} cut ($\cancel{E} < \cancel{E}_0$)	Jet substructure requirement	$M_{b\bar{b}}$ cut ($M_{b\bar{b}} > M_0$)		
		$b\bar{b}\nu\bar{\nu}$ (hZ)	0.178	0.164	0.161	0.160	0.124	0.014	0.013	0.012	0.012
$b\bar{b}\nu\bar{\nu}$ (ZZ)	1.45		0.495	0.473		0.368	0.014	0.127	0.124	0.120	0.007
$b\bar{b}\nu\bar{\nu}$ ($h\nu\bar{\nu}$)	318		95.5	4.50		0.614	0.347	187	1.42	1.03	0.897
$b\bar{b}\nu\bar{\nu}$ (tot)	641		222	10.9		4.00	0.538	351	4.75	3.97	1.44

Table 6: The effect of cut-flow on the cross-sections for various SM background subprocesses and the **total background** in two different final states ($N_{c\text{-jet}} = 1$ and $N_{c\text{-jet}} = 2$) at $\sqrt{s} = 3$ TeV.

BPs	Production cross-section (fb)	Cross sections (fb): $N_{c\text{-jet}} = 1$ final state				Cross sections (fb): $N_{c\text{-jet}} = 2$ final state					
		Basic Cuts	\cancel{E} cut ($\cancel{E} < \cancel{E}_0$)	Jet substructure requirement	$M_{b\bar{b}}$ cut ($M_{b\bar{b}} > M_0$)	Basic Cuts	\cancel{E} cut ($\cancel{E} < \cancel{E}_0$)	Jet substructure requirement	$M_{b\bar{b}}$ cut ($M_{b\bar{b}} > M_0$)		
		BP1	2.66	2.55	2.53	2.49	1.84	0.027	0.026	0.024	0.023
BP2	10.9		10.8	10.7		10.5	7.72	0.040	0.039	0.036	0.035
BP3	0.056		0.056	0.056		0.055	0.040	$\sim 10^{-4}$	$\sim 10^{-4}$	$\sim 10^{-4}$	$\sim 10^{-4}$
BP4	11.4		10.9	10.8		10.6	7.85	0.114	0.112	0.102	0.099
BP5	55.0		54.5	54.0		53.1	38.9	0.207	0.203	0.184	0.180
BP6	0.388		0.386	0.383		0.376	0.276	$\sim 6 \cdot 10^{-4}$	$\sim 6 \cdot 10^{-4}$	$\sim 6 \cdot 10^{-4}$	$\sim 6 \cdot 10^{-4}$

Table 7: The effect of cut-flow on the signal cross section for various representative benchmark points in two different final states ($N_{c\text{-jet}} = 1$ and $N_{c\text{-jet}} = 2$) at $\sqrt{s} = 10$ TeV assuming $\text{BR}(h \rightarrow b\bar{b}) = 1$.

Background processes	Production cross-section (fb)	Cross sections (fb): $N_{c\text{-jet}} = 1$ final state				Cross sections (fb): $N_{c\text{-jet}} = 2$ final state					
		Basic Cuts	\cancel{E} cut ($\cancel{E} < \cancel{E}_0$)	Jet substructure requirement	$M_{b\bar{b}}$ cut ($M_{b\bar{b}} > M_0$)	Basic Cuts	\cancel{E} cut ($\cancel{E} < \cancel{E}_0$)	Jet substructure requirement	$M_{b\bar{b}}$ cut ($M_{b\bar{b}} > M_0$)		
		$b\bar{b}\nu\bar{\nu}$ (hZ)	0.016	0.016	0.016	0.015	0.011	$< 10^{-5}$	$< 10^{-5}$	$< 10^{-5}$	$< 10^{-5}$
$b\bar{b}\nu\bar{\nu}$ (ZZ)	0.183		0.045	0.044		0.043	0.002	$\sim 2 \cdot 10^{-4}$	$\sim 2 \cdot 10^{-4}$	$\sim 2 \cdot 10^{-4}$	$< 10^{-4}$
$b\bar{b}\nu\bar{\nu}$ ($h\nu\bar{\nu}$)	540		167	0.717		0.588	0.451	246	0.079	0.077	0.073
$b\bar{b}\nu\bar{\nu}$ (tot)	1101		373	4.03		3.53	0.673	466	0.488	0.427	0.310

Table 8: The effect of cut-flow on the cross-sections for various SM background subprocesses and the **total background** in two different final states ($N_{c\text{-jet}} = 1$ and $N_{c\text{-jet}} = 2$) at $\sqrt{s} = 10$ TeV.

It is clear from the Tables 5 and 7 that at muon collider center-of-mass energies the signal events dominantly contribute in the *exactly one central-jet* final state than the other one because of the fact that it is a $2 \rightarrow 2$ process. Moreover, the contribution of signal events in *exactly one central-jet* final state increases with increasing mass of the heavy particle (VLL) in the t/u channel. This is evident if we compare the event rate after basic selection criteria for various benchmark points ($\{\text{BP1-BP3}\}$ or $\{\text{BP4-BP6}\}$) which corresponds to pVLL mass in the range $\{1-3\}$ TeV. This feature is also visible in Fig. 9.

For the background events coming from the $\mu^+ \mu^- \rightarrow hZ$ subprocess more than 92% of the events contribute to $N_{c\text{-jet}} = 1$ final state and the effects of cut-flow on these events are similar to that of the

signal events. The contribution of $\mu^+\mu^- \rightarrow ZZ$ subprocess to the $N_{c\text{-jet}} = 1$ final state is 34% (25%) of its production cross section and a very negligible fraction contributes in the $N_{c\text{-jet}} = 2$ final state at $\sqrt{s} = 3$ (10) TeV (see Table 6 and 8). This is because a large fraction of events coming from this subprocess contributes in zero central-jet events, as can be seen in Fig. 10. On the other hand, though $h\nu\bar{\nu}$ (and also $Z\nu\bar{\nu}$) contributes dominantly to $N_{c\text{-jet}} = 2$ final state, however, its contribution after applying the selection criteria mentioned earlier can be reduced substantially.

The effect of our selection criteria on the signal events is less severe in both the final states as can be seen from the cut-flow tables. Whereas one has a factor of $\sim \frac{1}{400}$ and $\frac{1}{550}$ suppression in the SM background rate in the *exactly one central-jet* final state after applying the combination of cuts mentioned in section 3.4 at $\sqrt{s} = 3$ TeV and 10 TeV, respectively. This factor for the *exactly two central-jet* final state is $\sim \frac{1}{250}$ for $\sqrt{s} = 3$ TeV and even larger at 10 TeV center-of-mass energy. The significant effect on the background comes from the missing energy cut as already explained in section 3.

The cut-flow tables corresponding to the signal events also suggest that the effect of the dark photon mass on the *kinematics*, in particular, on the cut efficiencies is very small as long as $m_{\gamma_d} \ll \sqrt{s}$. However, it plays a significant role in the estimation of the cross section as it depends on values of dark photon mass as well as the dark gauge coupling.

In Table 9, we quote the signal significances for 3 TeV and 10 TeV muon collider center-of-mass energies for various choices of our benchmark points for two different final states assuming an integrated luminosity of 100 fb^{-1} . To estimate the signal significance (σ) and set a 2σ exclusion limit we have used the following formula [89–91]

$$\sigma = \sqrt{2 \left(S - B \ln \left(1 + \frac{S}{B} \right) \right)}. \quad (31)$$

where, S is number of signal events and B is that for the background at a given integrated luminosity. While estimating the significance we have also taken into account the appropriate branching ratio (57%) for $h \rightarrow b\bar{b}$ decay to get the actual number of signal events.

BPs	Signal significance (σ)			
	$\sqrt{s} = 3 \text{ TeV}$		$\sqrt{s} = 10 \text{ TeV}$	
	$N_{c\text{-jet}} = 1$	$N_{c\text{-jet}} = 2$	$N_{c\text{-jet}} = 1$	$N_{c\text{-jet}} = 2$
BP1	24.6	8.34	9.12	0.23
BP2	38.5	11.1	24.6	0.35
BP3	0.34	0.04	0.27	—
BP4	56.4	16.6	24.9	0.96
BP5	92.2	23.6	62.9	1.67
BP6	2.14	0.14	1.78	—

Table 9: Estimated signal significance in the context of $\mu^+\mu^- \rightarrow h\gamma_d$ process in two different final states ($N_{c\text{-jet}} = 1$ and $N_{c\text{-jet}} = 2$) under consideration at two different muon collider center-of-mass energies ($\sqrt{s} = 3$ and 10 TeV) assuming an integrated luminosity of 100 fb^{-1} .

The increase in significance for BP2 compared to BP1 is due to higher signal cross section at this benchmark point even though the mass of the pVLL in the t/u -channel propagator is higher. Also one has a better estimate of the signal significance for the set of BPs corresponding to dark photon mass 50 GeV compared to that for dark photon mass 90 GeV as the cross section for $h\gamma_d$ production is expected to increase with decreasing dark photon mass.

In Fig. 17, we present the 2σ exclusion limit in the $m_{\gamma_d} - m_{\mu_p}$ plane at $\sqrt{s} = 3$ TeV assuming an integrated luminosity of 1 ab^{-1} in two different final states for two sets of g_d and $\sin\theta_L$ keeping $\sin\theta_s$

fixed at 0.05. The same at $\sqrt{s} = 10$ TeV and an integrated luminosity of 10 ab^{-1} is presented in Fig. 18. The Fig. 19 represents the 2σ exclusion limit in the $g_d - m_{\gamma_d}$ plane corresponding to $\sqrt{s} = 3$ TeV and an integrated luminosity of 1 ab^{-1} . The regions allowed by the constraint presented in Eq. (15) and the current muon $g - 2$ measurements at 1σ level are represented by the one above the dashed (black) and the solid (black) lines, respectively, in all these figures.

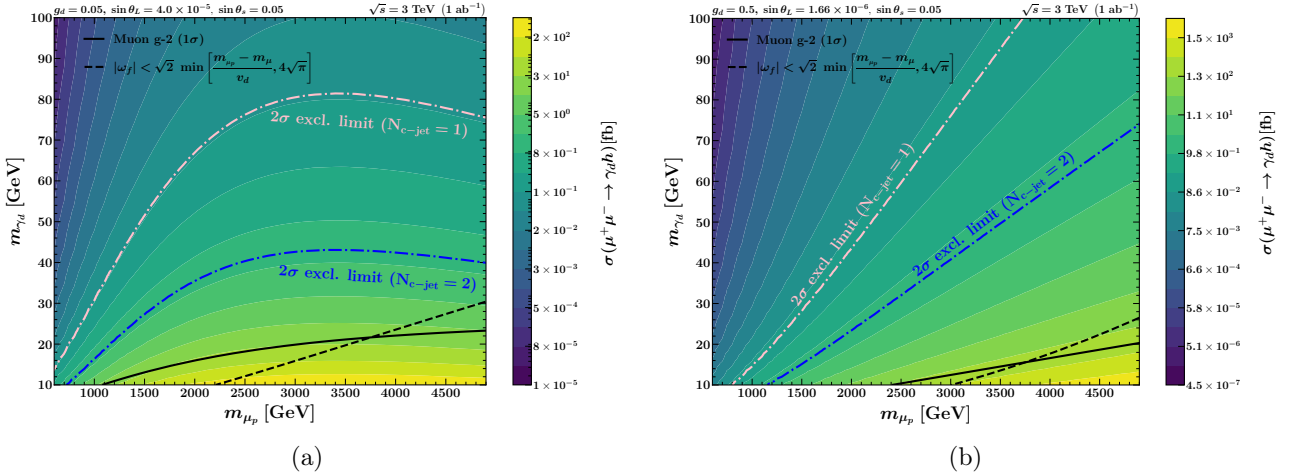


Figure 17: 2σ exclusion limit in the $m_{\gamma_d} - m_{\mu_p}$ plane for two different final states at 3 TeV muon collider center-of-mass energy for (a) $g_d = 0.05$, $\sin \theta_L = 4 \times 10^{-5}$, $\sin \theta_s = 0.05$ and (b) $g_d = 0.5$, $\sin \theta_L = 1.66 \times 10^{-6}$, $\sin \theta_s = 0.05$ assuming an integrated luminosity of 1 ab^{-1} . The exclusion limits in $N_{\text{c-jet}} = 1$ (pink) and $N_{\text{c-jet}} = 2$ (blue) final states are represented by the region below the dash-dot lines. The region above the dashed (black) line is allowed by the constraint represented in Eq. (15) while the muon $g - 2$ allowed region is represented by the one above solid (black) line.

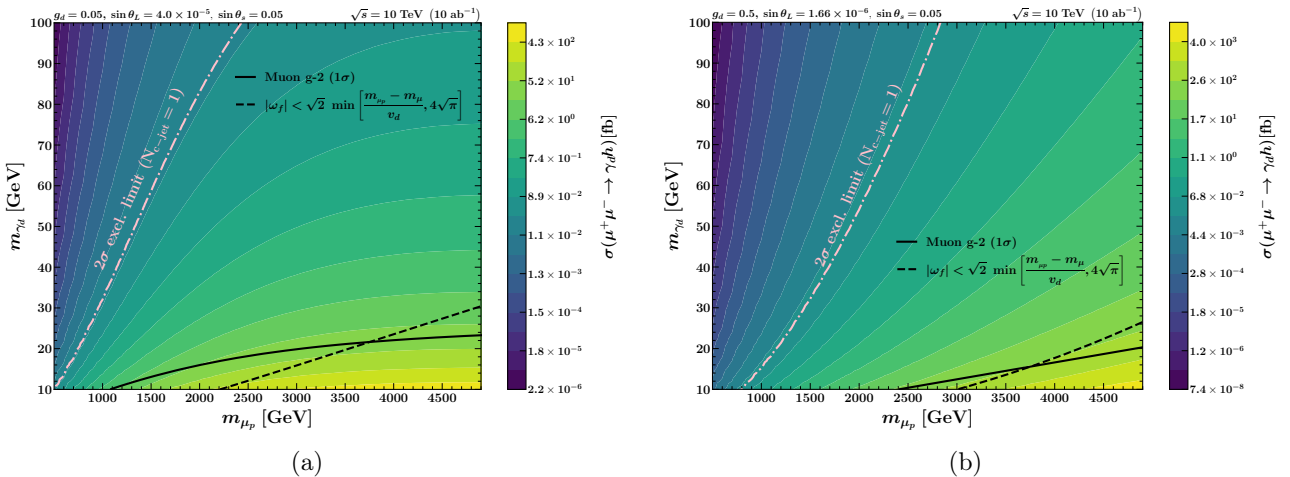


Figure 18: 2σ exclusion limit in the $m_{\gamma_d} - m_{\mu_p}$ plane in $N_{\text{c-jet}} = 1$ final state at 10 TeV muon collider center-of-mass energy for (a) $g_d = 0.05$, $\sin \theta_L = 4 \times 10^{-5}$, $\sin \theta_s = 0.05$ and (b) $g_d = 0.5$, $\sin \theta_L = 1.66 \times 10^{-6}$, $\sin \theta_s = 0.05$ assuming an integrated luminosity of 10 ab^{-1} . The 2σ exclusion limit is represented by dash-dot line (pink). The region above the dashed (black) line is allowed by the constraint represented in Eq. (15) while the muon $g - 2$ allowed region is represented by the one above solid (black) line.

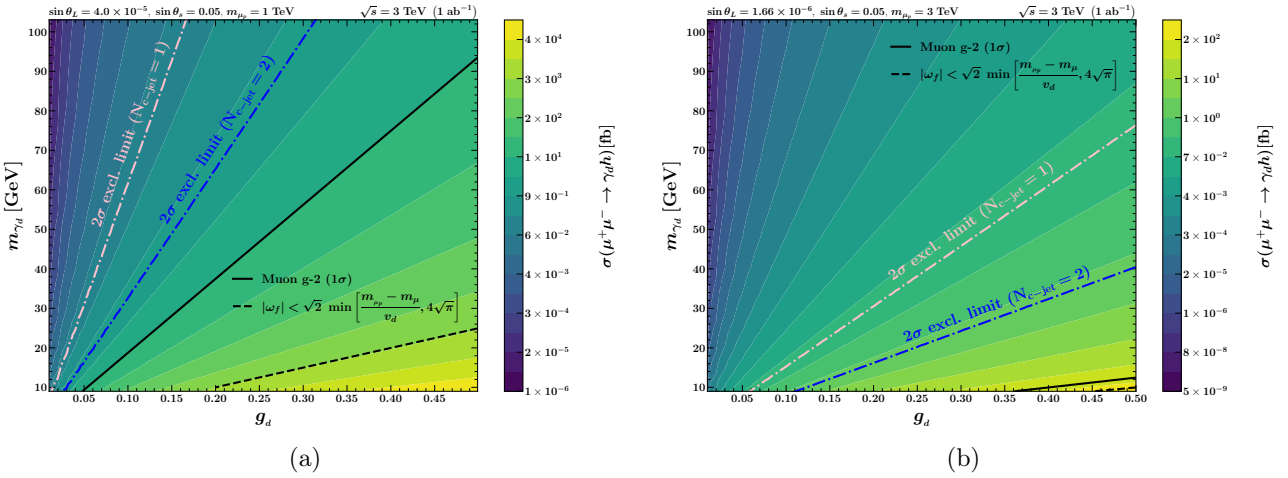


Figure 19: 2σ exclusion limit (represented by dashed-dot line) in the $g_d - m_{\gamma_d}$ plane using the data corresponding to $\sqrt{s} = 3$ TeV and an integrated luminosity of 1 ab^{-1} in the $N_{\text{c-jet}} = 1$ (pink) and $N_{\text{c-jet}} = 2$ (blue) final states for two different sets of $\sin \theta_L$ and m_{μ_p} : (a) $\sin \theta_L = 4 \times 10^{-5}$, $m_{\mu_p} = 1$ TeV and (b) $\sin \theta_L = 1.66 \times 10^{-6}$, $m_{\mu_p} = 3$ TeV. The region above the dashed (black) line is allowed by the constraint represented in Eq. (15) while the muon $g - 2$ allowed region is represented by the one above solid (black) line.

5 Conclusion

Motivated by the prospects of Higgs physics at proposed future lepton colliders and precise measurements of the Higgs properties, we have investigated the implications of a *portal vector-like lepton* on the Higgs production in association with a neutral gauge boson (Z/γ_d) at the proposed future muon collider experiment and its consequence on dark photon. In particular, we focus on the Higgs and dark photon associated production via t and u channel pVLL exchange in addition to the dark photon mediated s -channel contribution. To avoid constraints coming from the low energy flavor changing observables we consider pVLL mixing only with one generation of lepton family, in particular, the second generation charged lepton. We also present a detailed comparison of the $h\gamma_d$ production rate with that of the hZ production at muon collider. The later process is considered both in the context of SM and in presence of the portal VLL extension of the SM.

The $\mu^+ \mu^- \rightarrow h\gamma_d$ process is highly sensitive to the following independent model parameters: the dark photon mass (m_{γ_d}), dark gauge coupling (g_d), and both fermion ($\sin \theta_L$) and scalar ($\sin \theta_s$) mixing angles. We explore the *non-decoupling* effect owing to the presence of the muon-heavy muon-dark photon vertex and show that a significant region of parameter space consistent with the perturbative unitarity, electroweak precision measurements, lepton flavor universality, allowed ranges of scalar mixing angle and other relevant constraints can be found where the $h\gamma_d$ cross-section is \sim few fb to 10^2 fb. Consequently, one can achieve up to 10% better precision in the measurement of Higgs properties w.r.t. that achievable in the hZ channel.

A crucial outcome of our study is that this process not only provides an enhanced Higgs production rate at the muon collider but also helps to set a strong limit on the dark photon mass even for a fermion mixing angle as low as 10^{-6} , independent of the gauge kinetic mixing parameter.

We have proposed two final states, i.e., *leptonically quiet exactly one and exactly two central-jet(s) along with missing energy*. These final states originate from the $h\gamma_d$ process when the Higgs boson decays to a pair of bottom quarks and the dark photon is treated as an invisible particle at the detector. In order to set a 2σ exclusion limit in the $m_{\gamma_d} - m_{\mu_p}$ plane using the $h\gamma_d$ process in the aforementioned final states, we have also considered an exhaustive study of the SM background processes which contribute to these final states. With the help of certain kinematic variables such as missing energy, requirement of the presence of substructure in the leading central CA_{1.2} jet, and the invariant mass associated with the $b\bar{b}$ system to lie around the Higgs mass it is possible to substantially reduce the SM background contributions and efficiently isolate the signal of $h\gamma_d$ production at the

future muon collider.

A 2σ exclusion limit upto $m_{\gamma_d} = 80$ (76) GeV can be obtained using our analysis in the *exactly one central-jet plus missing energy* final state at 3 TeV muon collider center-of-mass energy for $g_d = 0.05$ (0.5), $\sin \theta_L = 4 \times 10^{-5}$ (1.66×10^{-6}), $\sin \theta_s = 0.05$ for a heavy muon mass $m_{\mu_p} \sim 3$ TeV. The corresponding bounds in the *exactly two central-jets plus missing energy* final state are $m_{\gamma_d} = 43$ GeV and 46 GeV for a heavy muon mass $m_{\mu_p} \sim 3.3$ TeV using the same set of choices of the other parameters as mentioned above. We also present the 2σ exclusion limit for the *exactly one central-jet plus missing energy* final state in the m_{μ_p} – m_{γ_d} plane for a higher-energy muon collider scenario with $\sqrt{s} = 10$ TeV and corresponding integrated luminosity of 10 ab^{-1} . Assuming $m_{\mu_p} = 1$ TeV, $\sin \theta_L = 4 \times 10^{-5}$ and $\sin \theta_s = 0.05$ one can exclude the value of the dark gauge coupling above 0.15 (0.28) for $m_{\gamma_d} \leq 90$ GeV at $\sqrt{s} = 3$ TeV with an integrated luminosity of 1 ab^{-1} in the *exactly one (two) central-jet(s) plus missing energy* final state. The corresponding limits on g_d for $m_{\mu_p} = 3$ TeV, $\sin \theta_L = 1.66 \times 10^{-6}$, $\sin \theta_s = 0.05$ and $m_{\gamma_d} < 40$ GeV are respectively 0.26 and 0.5 for these two final states assuming the same muon collider collision energy and integrated luminosity. Thus a large region of parameter space consistent with latest muon $g - 2$ measurement both in the g_d – m_{γ_d} and m_{μ_p} – m_{γ_d} planes can be probed at the future muon collider facilities using the Higgs associated production with a dark photon as presented in this article.

Acknowledgement

We gratefully acknowledge Satyanarayan Mukhopadhyay for his valuable insights and useful comments. KT thanks the Department of Science and Technology (DST), Government of India, for financial support under the INSPIRE Fellowship Programme (IF220170). KT is also grateful to Sujay Mondal for providing access to high-performance computational facilities which significantly aided the progress of this work. KT further extends her thanks to the organizers and instructors of the Iwate Collider School 2025 for their excellent lectures and tutorial sessions. SV acknowledges the Physical Research Laboratory, Ahmedabad, for supporting him through the Post-Doctoral Fellowship.

A Vertex factors

In this appendix, we present Feynman rules for the relevant vertices assuming all the associated four momenta are coming out of the vertex. Below the L and R represent the *left- and right- chiral* fermions, respectively.

A.1 Vertices with Dark Photon:

$$1. \mu_{p_R}^+ - \mu_L^- - \gamma_d / \mu_R^+ - \mu_{p_L}^- - \gamma_d$$

$$\text{VF}_1 = -ig_d \sin \theta_L \cos \theta_L \gamma^\mu \quad (\text{A.1})$$

$$2. \mu_{p_L}^+ - \mu_R^- - \gamma_d / \mu_L^+ - \mu_{p_R}^- - \gamma_d$$

$$\text{VF}_2 = -ig_d \sin \theta_R \cos \theta_R \gamma^\mu \quad (\text{A.2})$$

$$3. \mu_L^+ - \mu_R^- - \gamma_d$$

$$\text{VF}_3 = -ig_d \sin^2 \theta_R \gamma^\mu \quad (\text{A.3})$$

$$4. \mu_R^+ - \mu_L^- - \gamma_d$$

$$\text{VF}_4 = -ig_d \sin^2 \theta_L \gamma^\mu \quad (\text{A.4})$$

A.2 Vertices with Z boson:

1. $\mu_{p_R}^+ - \mu_L^- - Z / \mu_R^+ - \mu_{p_L}^- - Z$

$$VF_5 = -\frac{i}{2} g_z \sin \theta_L \cos \theta_L \gamma^\mu \quad (A.5)$$

2. $\mu_L^+ - \mu_R^- - Z$

$$VF_6 = i g_z \sin^2 \theta_W \gamma^\mu \quad (A.6)$$

3. $\mu_R^+ - \mu_L^- - Z$

$$VF_7 = i \frac{g_z}{2} (2 \sin^2 \theta_W - \cos^2 \theta_L) \gamma^\mu \quad (A.7)$$

A.3 Vertices with Higgs:

1. $\mu_{p_L}^+ - \mu_L^- - h / \mu_R^+ - \mu_{p_R}^- - h$

$$VF_8 = -\frac{i}{\sqrt{2}} \sin \theta_R (\sin \theta_L \sin \theta_s \omega_f + \cos \theta_L \cos \theta_s y_m) \quad (A.8)$$

2. $\mu_{p_R}^+ - \mu_R^- - h / \mu_L^+ - \mu_{p_L}^- - h$

$$VF_9 = \frac{i}{\sqrt{2}} \cos \theta_R (\cos \theta_L \sin \theta_s \omega_f - \sin \theta_L \cos \theta_s y_m) \quad (A.9)$$

3. $\gamma_d - \gamma_d - h$

$$VF_{10} = -2 i g_d m_{\gamma_d} \sin \theta_s \quad (A.10)$$

4. $Z - Z - h$

$$VF_{11} = i g_z m_z \cos \theta_s \quad (A.11)$$

B Squared matrix element for $\mu^+ \mu^- \rightarrow h \gamma_d$

The t - and u - channel diagrams for the $\mu^+ \mu^- \rightarrow h \gamma_d$ process via portal vector-like lepton mediation (μ_p) are presented in Fig 20.

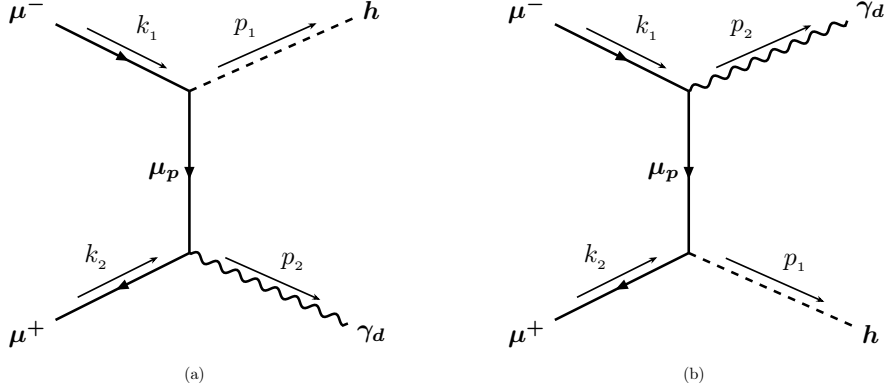


Figure 20: Feynman diagrams for the process $\mu^+ \mu^- \rightarrow h \gamma_d$ mediated by the portal matter m_{μ_p} through the (a) t -channel and (b) u -channel.

The amplitude for the t -channel diagram is given by

$$i\mathcal{M}_t = -i \left[\bar{v}_{s_2}(k_2) \gamma^\mu (c_V^t + c_A^t \gamma^5) \epsilon_\mu^{*\lambda}(\vec{p}_2) \frac{(\not{k}_1 - \not{p}_1 + m_{\mu_p})}{(k_1 - p_1)^2 - m_{\mu_p}^2} (c_s^t + c_p^t \gamma^5) u_{s_1}(k_1) \right] \quad (\text{B.1})$$

where c_s^t , c_p^t , c_V^t and c_A^t are given by

$$\begin{aligned} c_s^t &= \frac{m_{\mu_p}}{4} \sin 2\theta_L \left[\frac{1}{D^2} \frac{g_d}{m_{\gamma_d}} \sin \theta_s \left(1 - \frac{m_\mu^2}{m_{\mu_p}^2} \right) (\sin^2 \theta_L - \frac{m_\mu}{m_{\mu_p}} \cos^2 \theta_L) + \frac{1}{v_{\text{EW}}} \cos \theta_s \left(1 + \frac{m_\mu}{m_{\mu_p}} \right) \right] \\ c_p^t &= -\frac{m_{\mu_p}}{4} \sin 2\theta_L \left[\frac{1}{D^2} \frac{g_d}{m_{\gamma_d}} \sin \theta_s \left(1 - \frac{m_\mu^2}{m_{\mu_p}^2} \right) (\sin^2 \theta_L + \frac{m_\mu}{m_{\mu_p}} \cos^2 \theta_L) + \frac{1}{v_{\text{EW}}} \cos \theta_s \left(1 - \frac{m_\mu}{m_{\mu_p}} \right) \right] \\ c_V^t &= \frac{g_d}{2} \cos \theta_L \sin \theta_L \left(\frac{m_\mu}{m_{\mu_p}} \frac{1}{D^2} + 1 \right) \\ c_A^t &= \frac{g_d}{2} \cos \theta_L \sin \theta_L \left(\frac{m_\mu}{m_{\mu_p}} \frac{1}{D^2} - 1 \right) \end{aligned}$$

The amplitude of the u -channel diagram is given by

$$i\mathcal{M}_u = -i \left[\bar{v}_{s_2}(k_2) (c_s^u + c_p^u \gamma^5) \frac{(\not{p}_1 - \not{k}_2 + m_{\mu_p})}{(p_1 - k_2)^2 - m_{\mu_p}^2} \gamma^\mu (c_V^u + c_A^u \gamma^5) \epsilon_\mu^{*\lambda}(\vec{p}_2) u_{s_1}(k_1) \right] \quad (\text{B.2})$$

where c_s^u , c_p^u , c_V^u and c_A^u are given by

$$\begin{aligned} c_s^u &= \frac{m_{\mu_p}}{4} \sin 2\theta_L \left[\frac{1}{D^2} \frac{g_d}{m_{\gamma_d}} \sin \theta_s \left(1 - \frac{m_\mu^2}{m_{\mu_p}^2} \right) (\sin^2 \theta_L - \frac{m_\mu}{m_{\mu_p}} \cos^2 \theta_L) + \frac{1}{v_{\text{EW}}} \cos \theta_s \left(1 + \frac{m_\mu}{m_{\mu_p}} \right) \right] \\ c_p^u &= \frac{m_{\mu_p}}{4} \sin 2\theta_L \left[\frac{1}{D^2} \frac{g_d}{m_{\gamma_d}} \sin \theta_s \left(1 - \frac{m_\mu^2}{m_{\mu_p}^2} \right) (\sin^2 \theta_L + \frac{m_\mu}{m_{\mu_p}} \cos^2 \theta_L) + \frac{1}{v_{\text{EW}}} \cos \theta_s \left(1 - \frac{m_\mu}{m_{\mu_p}} \right) \right] \\ c_V^u &= \frac{g_d}{2} \cos \theta_L \sin \theta_L \left(\frac{m_\mu}{m_{\mu_p}} \frac{1}{D^2} + 1 \right) \\ c_A^u &= \frac{g_d}{2} \cos \theta_L \sin \theta_L \left(\frac{m_\mu}{m_{\mu_p}} \frac{1}{D^2} - 1 \right) \end{aligned}$$

The spin-averaged squared amplitude, neglecting the s channel dark photon mediated and t/u channel muon mediated contribution, is

$$\overline{|\mathcal{M}|^2} = |\mathcal{M}_t|^2 + |\mathcal{M}_u|^2 + 2 \text{Re}(\overline{\mathcal{M}_t \mathcal{M}_u^*}) \quad (\text{B.3})$$

where the t -channel contribution in the limit $m_\mu \rightarrow 0$ is

$$\begin{aligned} \overline{|\mathcal{M}_t|^2} &= \frac{2}{\left[(k_1 - p_1)^2 - m_{\mu_p}^2\right]^2} \left[A_1 \left\{ 2(k_1 \cdot p_1)(k_2 \cdot p_1) - p_1^2(k_1 \cdot k_2) \right\} + A_2 m_{\mu_p}^2 (k_1 \cdot k_2) \right. \\ &\quad + \frac{1}{m_{\gamma_d}^2} \left(A_1 \left\{ 2(k_1 \cdot p_1)(k_2 \cdot p_2)(p_1 \cdot p_2) - p_1^2(k_1 \cdot p_2)(k_2 \cdot p_2) - p_2^2(k_1 \cdot p_1)(k_2 \cdot p_1) \right. \right. \\ &\quad \left. \left. + \frac{p_1^2 p_2^2}{2} (k_1 \cdot k_2) \right\} + A_2 m_{\mu_p}^2 \left\{ (k_1 \cdot p_2)(k_2 \cdot p_2) - \frac{p_2^2}{2} (k_1 \cdot k_2) \right\} \right) \right] \end{aligned} \quad (\text{B.4})$$

Similarly, the u -channel contribution in the same limit reads

$$\begin{aligned} \overline{|\mathcal{M}_u|^2} &= \frac{2}{\left[(p_1 - k_2)^2 - m_{\mu_p}^2\right]^2} \left[A_1 \left\{ 2(k_1 \cdot p_1)(k_2 \cdot p_1) - p_1^2(k_1 \cdot k_2) \right\} + A_2 m_{\mu_p}^2 (k_1 \cdot k_2) \right. \\ &\quad + \frac{1}{m_{\gamma_d}^2} \left(A_1 \left\{ 2(k_1 \cdot p_2)(k_2 \cdot p_1)(p_1 \cdot p_2) - p_1^2(k_1 \cdot p_2)(k_2 \cdot p_2) - p_2^2(k_1 \cdot p_1)(k_2 \cdot p_1) \right. \right. \\ &\quad \left. \left. + \frac{p_1^2 p_2^2}{2} (k_1 \cdot k_2) \right\} + A_2 m_{\mu_p}^2 \left\{ (k_1 \cdot p_2)(k_2 \cdot p_2) - \frac{p_2^2}{2} (k_1 \cdot k_2) \right\} \right) \right] \end{aligned} \quad (\text{B.5})$$

Here, the coefficients A_1 and A_2 are as follows

$$\begin{aligned} A_1 &= (c_V^2 + c_A^2)(c_s^2 + c_p^2) - 4c_s c_p c_V c_A \\ A_2 &= (c_V^2 + c_A^2)(c_s^2 + c_p^2) + 4c_s c_p c_V c_A \end{aligned} \quad (\text{B.6})$$

with the coupling identifications

$$c_s = c_s^t = c_s^u, \quad c_p = c_p^t = -c_p^u, \quad c_V = c_V^t = c_V^u, \quad c_A = c_A^t = c_A^u.$$

The corresponding interference term is

$$\begin{aligned} \overline{\mathcal{M}_t \mathcal{M}_u^*} &= \frac{2}{\left[(k_1 - p_1)^2 - m_{\mu_p}^2\right] \left[(p_1 - k_2)^2 - m_{\mu_p}^2\right]} \left[2A_3 (k_1 \cdot p_1)(k_2 \cdot p_1) + A_2 m_{\mu_p}^2 (k_1 \cdot k_2) \right. \\ &\quad - \frac{1}{m_{\gamma_d}^2} \left(A_3 \left\{ p_1^2(k_1 \cdot p_2)(k_2 \cdot p_1) + p_2^2(k_1 \cdot p_1)(k_2 \cdot p_1) - (p_1 \cdot p_2)(k_1 \cdot p_2)(k_2 \cdot p_1) \right. \right. \\ &\quad \left. \left. - (p_1 \cdot p_2)(k_1 \cdot p_1)(k_2 \cdot p_2) + (p_1 \cdot p_2)^2(k_1 \cdot k_2) - \frac{p_1^2 p_2^2}{2} (k_1 \cdot k_2) \right\} \right. \\ &\quad \left. + \frac{A_2}{2} m_{\mu_p}^2 \left\{ p_2^2(k_1 \cdot k_2) - (k_1 \cdot p_2)(k_2 \cdot p_2) \right\} \right) \right] \end{aligned} \quad (\text{B.7})$$

where the coefficient A_3 takes the form

$$A_3 = (c_s^2 - c_p^2)(c_V^2 - c_A^2) \quad (\text{B.8})$$

In the center-of-mass frame and in the limit $m_h, m_{\gamma_d} \ll E_{\text{CM}}$, the $\overline{|\mathcal{M}|^2}$ for the pure t - and u -channels and the corresponding interference contribution take the form

$$\begin{aligned} \overline{|\mathcal{M}_t|^2} &= \frac{E_{\text{CM}}^2}{(a - b \cos \theta)^2} \left[A_1 \left(\frac{E_{\text{CM}}^2}{4} \sin^2 \theta - m_h^2 \right) + A_2 m_{\mu_p}^2 + \frac{1}{2m_{\gamma_d}^2} \left(A_1 \left\{ \frac{E_{\text{CM}}^4}{4} (1 - \cos \theta)^2 \right. \right. \right. \\ &\quad \left. \left. \left. - \frac{(m_h^2 + m_{\gamma_d}^2) E_{\text{CM}}^2}{4} \sin^2 \theta + m_h^2 m_{\gamma_d}^2 \right\} + A_2 m_{\mu_p}^2 \left\{ \frac{E_{\text{CM}}^2}{4} \sin^2 \theta - m_{\gamma_d}^2 \right\} \right) \right] \end{aligned} \quad (\text{B.9})$$

$$\overline{|\mathcal{M}_u|^2} = \frac{E_{\text{CM}}^2}{(a + b \cos \theta)^2} \left[A_1 \left(\frac{E_{\text{CM}}^2}{4} \sin^2 \theta - m_h^2 \right) + A_2 m_{\mu_p}^2 + \frac{1}{2m_{\gamma_d}^2} \left(A_1 \left\{ \frac{E_{\text{CM}}^4}{4} (1 + \cos \theta)^2 \right. \right. \right. \\ \left. \left. \left. - \frac{(m_h^2 + m_{\gamma_d}^2) E_{\text{CM}}^2}{4} \sin^2 \theta + m_h^2 m_{\gamma_d}^2 \right\} + A_2 m_{\mu_p}^2 \left\{ \frac{E_{\text{CM}}^2}{4} \sin^2 \theta - m_{\gamma_d}^2 \right\} \right) \right] \quad (\text{B.10})$$

$$\overline{\mathcal{M}_t \mathcal{M}_u^*} = \frac{E_{\text{CM}}^2}{(a^2 - b^2 \cos^2 \theta)} \left[\left(A_3 \frac{E_{\text{CM}}^2}{4} \sin^2 \theta + A_2 m_{\mu_p}^2 \right) + \frac{1}{2m_{\gamma_d}^2} \left(A_3 \left\{ m_h^2 m_{\gamma_d}^2 \right. \right. \right. \\ \left. \left. \left. - \frac{(E_{\text{CM}}^2 + m_h^2 + m_{\gamma_d}^2) E_{\text{CM}}^2}{4} \sin^2 \theta \right\} + A_2 m_{\mu_p}^2 \left\{ \frac{E_{\text{CM}}^2}{8} \sin^2 \theta - m_{\gamma_d}^2 \right\} \right) \right] \quad (\text{B.11})$$

Here,

$$a = \frac{E_{\text{CM}}^2}{2} + m_{\mu_p}^2, \quad b = \frac{E_{\text{CM}}^2}{2}.$$

References

- [1] ATLAS collaboration, G. Aad et al., *Observation of a new particle in the search for the Standard Model Higgs boson with the ATLAS detector at the LHC*, *Phys. Lett. B* **716** (2012) 1–29, [[1207.7214](#)].
- [2] CMS collaboration, S. Chatrchyan et al., *Observation of a New Boson at a Mass of 125 GeV with the CMS Experiment at the LHC*, *Phys. Lett. B* **716** (2012) 30–61, [[1207.7235](#)].
- [3] W. Kilian, M. Kramer and P. M. Zerwas, *Higgsstrahlung and W W fusion in e+ e- collisions*, *Phys. Lett. B* **373** (1996) 135–140, [[hep-ph/9512355](#)].
- [4] Z. Liu, L.-T. Wang and H. Zhang, *Exotic decays of the 125 GeV Higgs boson at future e+e- lepton colliders*, *Chin. Phys. C* **41** (2017) 063102, [[1612.09284](#)].
- [5] A. G. Akeroyd, A. Arhrib and M. Capdequi Peyranere, *CP odd Higgs boson production in association with neutral gauge boson in high-energy e+ e- collisions*, *Mod. Phys. Lett. A* **14** (1999) 2093–2108, [[hep-ph/9907542](#)].
- [6] S. Kanemura, *Possible enhancement of the e+ e- → H+- W+ cross-section in the two Higgs doublet model*, *Eur. Phys. J. C* **17** (2000) 473–486, [[hep-ph/9911541](#)].
- [7] B. A. Ouazghour, A. Arhrib, K. Cheung, E.-s. Ghourmin and L. Rahili, *Associated charged Higgs boson production within the 2HDM: e-e+ versus μ-μ+ colliders*, *Phys. Rev. D* **110** (2024) 095026, [[2408.13952](#)].
- [8] LEP WORKING GROUP FOR HIGGS BOSON SEARCHES, ALEPH, DELPHI, L3, OPAL collaboration, R. Barate et al., *Search for the standard model Higgs boson at LEP*, *Phys. Lett. B* **565** (2003) 61–75, [[hep-ex/0306033](#)].
- [9] OPAL collaboration, G. Abbiendi et al., *Search for the standard model Higgs boson with the OPAL detector at LEP*, *Eur. Phys. J. C* **26** (2003) 479–503, [[hep-ex/0209078](#)].
- [10] FCC collaboration, A. Abada et al., *FCC-ee: The Lepton Collider: Future Circular Collider Conceptual Design Report Volume 2*, *Eur. Phys. J. ST* **228** (2019) 261–623.
- [11] H. Abramowicz et al., *Higgs physics at the CLIC electron-positron linear collider*, *Eur. Phys. J. C* **77** (2017) 475, [[1608.07538](#)].

[12] R. Franceschini and M. Greco, *Higgs and BSM Physics at the Future Muon Collider*, *Symmetry* **13** (2021) 851, [[2104.05770](#)].

[13] Y. Hamada, R. Kitano, R. Matsudo, S. Okawa, R. Takai, H. Takaura et al., *Higgs boson production at $\mu+\mu+$ colliders*, *Phys. Rev. D* **110** (2024) 113011, [[2408.01068](#)].

[14] E. J. Chun and T. Mondal, *Explaining $g-2$ anomalies in two Higgs doublet model with vector-like leptons*, *JHEP* **11** (2020) 077, [[2009.08314](#)].

[15] P. Asadi, S. Homiller, A. Radick and T.-T. Yu, *Fermion-portal dark matter at a high-energy muon collider*, *Phys. Rev. D* **112** (2025) 055038, [[2412.14235](#)].

[16] A. Crivellin, F. Kirk, C. A. Manzari and M. Montull, *Global Electroweak Fit and Vector-Like Leptons in Light of the Cabibbo Angle Anomaly*, *JHEP* **12** (2020) 166, [[2008.01113](#)].

[17] M. Kirk, *Cabibbo anomaly versus electroweak precision tests: An exploration of extensions of the Standard Model*, *Phys. Rev. D* **103** (2021) 035004, [[2008.03261](#)].

[18] G. N. Wojcik, L. L. Everett, S. T. Eu and R. Ximenes, *Lepton flavor portal matter*, *Phys. Rev. D* **108** (2023) 055033, [[2303.12983](#)].

[19] Z. Poh and S. Raby, *Vectorlike leptons: Muon $g-2$ anomaly, lepton flavor violation, Higgs boson decays, and lepton nonuniversality*, *Phys. Rev. D* **96** (2017) 015032, [[1705.07007](#)].

[20] R. Dermisek, K. Hermanek and N. McGinnis, *Muon $g-2$ in two-Higgs-doublet models with vectorlike leptons*, *Phys. Rev. D* **104** (2021) 055033, [[2103.05645](#)].

[21] H. M. Lee, J. Song and K. Yamashita, *Seesaw lepton masses and muon $g-2$ from heavy vector-like leptons*, *J. Korean Phys. Soc.* **79** (2021) 1121–1134, [[2110.09942](#)].

[22] J. Kawamura, S. Raby and A. Trautner, *Complete vectorlike fourth family with $U(1)'$: A global analysis*, *Phys. Rev. D* **101** (2020) 035026, [[1911.11075](#)].

[23] M. Endo and S. Mishima, *Muon $g-2$ and CKM unitarity in extra lepton models*, *JHEP* **08** (2020) 004, [[2005.03933](#)].

[24] C. A. Manzari, *Vector-Like Leptons in Light of the Cabibbo-Angle Anomaly*, in *Beyond Standard Model: From Theory to Experiment*, 5, 2021. [2105.03399](#).

[25] B. Capdevila, A. Crivellin, C. A. Manzari and M. Montull, *Explaining $b \rightarrow s\ell^+\ell^-$ and the Cabibbo angle anomaly with a vector triplet*, *Phys. Rev. D* **103** (2021) 015032, [[2005.13542](#)].

[26] W. Abdallah, M. Ashry, J. Kawamura and A. Moursy, *Semivisible dark photon in a model with vectorlike leptons for the $(g-2)e, \mu$ and W -boson mass anomalies*, *Phys. Rev. D* **109** (2024) 015031, [[2308.05691](#)].

[27] H. M. Lee and K. Yamashita, *A model of vector-like leptons for the muon $g-2$ and the W boson mass*, *Eur. Phys. J. C* **82** (2022) 661, [[2204.05024](#)].

[28] C.-H. Lee and R. N. Mohapatra, *Vector-Like Quarks and Leptons, $SU(5) \otimes SU(5)$ Grand Unification, and Proton Decay*, *JHEP* **02** (2017) 080, [[1611.05478](#)].

[29] F. Gursey, P. Ramond and P. Sikivie, *A Universal Gauge Theory Model Based on $E6$* , *Phys. Lett. B* **60** (1976) 177–180.

[30] B. Kyae and C. S. Shin, *Vector-like leptons and extra gauge symmetry for the natural Higgs boson*, *JHEP* **06** (2013) 102, [[1303.6703](#)].

[31] M. Cvetic, G. Shiu and A. M. Uranga, *Three family supersymmetric standard - like models from intersecting brane worlds*, *Phys. Rev. Lett.* **87** (2001) 201801, [[hep-th/0107143](#)].

[32] G. B. Cleaver, A. E. Faraggi, D. V. Nanopoulos and J. W. Walker, *Phenomenological study of a minimal superstring standard model*, *Nucl. Phys. B* **593** (2001) 471–504, [[hep-ph/9910230](#)].

[33] F. Marchesano, D. Regalado and L. Vazquez-Mercado, *Discrete flavor symmetries in D-brane models*, *JHEP* **09** (2013) 028, [[1306.1284](#)].

[34] ATLAS collaboration, G. Aad et al., *Search for vector-like leptons coupling to first- and second-generation Standard Model leptons in pp collisions at $\sqrt{s} = 13$ TeV with the ATLAS detector*, *JHEP* **05** (2025) 075, [[2411.07143](#)].

[35] CMS collaboration, A. Tumasyan et al., *Search for pair-produced vector-like leptons in final states with third-generation leptons and at least three b quark jets in proton-proton collisions at $s=13$ TeV*, *Phys. Lett. B* **846** (2023) 137713, [[2208.09700](#)].

[36] CMS collaboration, A. M. Sirunyan et al., *Search for vector-like leptons in multilepton final states in proton-proton collisions at $\sqrt{s} = 13$ TeV*, *Phys. Rev. D* **100** (2019) 052003, [[1905.10853](#)].

[37] C.-X. Yue, Y.-Q. Wang, H. Wang, Y.-H. Wang and S. Li, *Searching for singlet vector-like leptons via pair production at ILC*, *Nucl. Phys. B* **1000** (2024) 116482, [[2402.02072](#)].

[38] L. Shang, M. Wang, Z. Heng and B. Yang, *Search for the singlet vector-like lepton at future e^+e^- colliders*, *Eur. Phys. J. C* **81** (2021) 415.

[39] Q. Guo, L. Gao, Y. Mao and Q. Li, *Vector-like lepton searches at a muon collider in the context of the 4321 model*, *Chin. Phys. C* **47** (2023) 103106, [[2304.01885](#)].

[40] N. Ghosh, S. K. Rai and T. Samui, *Search for a leptoquark and vector-like lepton in a muon collider*, *Nucl. Phys. B* **1004** (2024) 116564, [[2309.07583](#)].

[41] P. N. Bhattacharjee and S. P. Martin, *Prospects for vectorlike leptons at future proton-proton colliders*, *Phys. Rev. D* **100** (2019) 015033, [[1905.00498](#)].

[42] T. G. Rizzo, *Portal Matter and Dark Sector Phenomenology at Colliders*, in *Snowmass 2021*, 2, 2022. [2202.02222](#).

[43] T. D. Rueter and T. G. Rizzo, *Towards A UV-Model of Kinetic Mixing and Portal Matter*, *Phys. Rev. D* **101** (2020) 015014, [[1909.09160](#)].

[44] T. G. Rizzo, *Kinetic Mixing and Portal Matter Phenomenology*, *Phys. Rev. D* **99** (2019) 115024, [[1810.07531](#)].

[45] A. Belyaev, L. Panizzi, N. Thongyoi and F. Wilhelm, *The Muonic Portal to Vector Dark Matter: connecting precision muon physics, cosmology, and colliders*, [2510.18564](#).

[46] J. Lahiri, D. Pradhan and A. Sarkar, *The influence of lepton portal on the WIMP-pFIMP framework*, *JHEP* **08** (2025) 019, [[2410.19734](#)].

[47] J. P. Delahaye, M. Diemoz, K. Long, B. Mansoulié, N. Pastrone, L. Rivkin et al., *Muon Colliders*, [1901.06150](#).

[48] INTERNATIONAL MUON COLLIDER collaboration, D. Schulte, *The Muon Collider*, *JACoW IPAC2022* (2022) 821–826.

[49] K. M. Black et al., *Muon Collider Forum report*, *JINST* **19** (2024) T02015, [[2209.01318](#)].

[50] INTERNATIONAL MUON COLLIDER collaboration, C. Accettura et al., *Interim report for the International Muon Collider Collaboration (IMCC)*, *CERN Yellow Rep. Monogr. 2/2024* (2024) 176, [[2407.12450](#)].

[51] B. Holdom, *Searching for ϵ Charges and a New $U(1)$* , *Phys. Lett. B* **178** (1986) 65–70.

- [52] P. Fayet, *Extra $U(1)$'s and New Forces*, *Nucl. Phys. B* **347** (1990) 743–768.
- [53] M. Fabbrichesi, E. Gabrielli and G. Lanfranchi, *The Dark Photon*, [2005.01515](#).
- [54] J. Alexander et al., *Dark Sectors 2016 Workshop: Community Report*, tech. rep., Fermi National Accelerator Laboratory (FNAL), Batavia, IL (United States), 8, 2016.
- [55] J. H. Kim, S. D. Lane, H.-S. Lee, I. M. Lewis and M. Sullivan, *Searching for Dark Photons with Maverick Top Partners*, *Phys. Rev. D* **101** (2020) 035041, [[1904.05893](#)].
- [56] M. Bauer, P. Foldenauer and J. Jaeckel, *Hunting All the Hidden Photons*, *JHEP* **07** (2018) 094, [[1803.05466](#)].
- [57] APEX collaboration, D. He et al., *Dark photon constraints from a 7.139 GHz cavity haloscope experiment*, *Phys. Rev. D* **110** (2024) L021101, [[2404.00908](#)].
- [58] T. Robens and T. Stefaniak, *Status of the Higgs Singlet Extension of the Standard Model after LHC Run 1*, *Eur. Phys. J. C* **75** (2015) 104, [[1501.02234](#)].
- [59] T. Robens, *Investigating extended scalar sectors at current and future colliders*, *PoS LHCP2019* (2019) 138, [[1908.10809](#)].
- [60] T. Robens, *More Doublets and Singlets*, in *56th Rencontres de Moriond on Electroweak Interactions and Unified Theories*, 5, 2022. [2205.06295](#).
- [61] S. Adhikari, S. D. Lane, I. M. Lewis and M. Sullivan, *Complex Scalar Singlet Model Benchmarks for Snowmass*, in *Snowmass 2021*, 3, 2022. [2203.07455](#).
- [62] S. D. Lane, I. M. Lewis and M. Sullivan, *Resonant multiscalar production in the generic complex singlet model in the multi-TeV region*, *Phys. Rev. D* **110** (2024) 055017, [[2403.18003](#)].
- [63] T. Robens, *Constraining extended scalar sectors at current and future colliders - an update*, in *8th Workshop on Theory, Phenomenology and Experiments in Flavour Physics: Neutrinos, Flavor Physics and Beyond*, 9, 2022. [2209.15544](#).
- [64] T. Robens and R. Santos, *BSM: Extended Scalar Sectors*, tech. rep., Boskovic Inst., Zagreb, CERN, 7, 2025.
- [65] ATLAS collaboration, G. Aad et al., *Combination of searches for invisible decays of the Higgs boson using 139 fb^{-1} of proton-proton collision data at $s=13$ TeV collected with the ATLAS experiment*, *Phys. Lett. B* **842** (2023) 137963, [[2301.10731](#)].
- [66] CMS collaboration, A. Tumasyan et al., *A search for decays of the Higgs boson to invisible particles in events with a top-antitop quark pair or a vector boson in proton-proton collisions at $\sqrt{s} = 13$ TeV*, *Eur. Phys. J. C* **83** (2023) 933, [[2303.01214](#)].
- [67] A. Papaefstathiou, T. Robens and G. White, *Signal strength and W-boson mass measurements as a probe of the electro-weak phase transition at colliders - Snowmass White Paper*, in *Snowmass 2021*, 5, 2022. [2205.14379](#).
- [68] ALEPH, DELPHI, L3, OPAL, SLD, LEP ELECTROWEAK WORKING GROUP, SLD ELECTROWEAK GROUP, SLD HEAVY FLAVOUR GROUP collaboration, S. Schael et al., *Precision electroweak measurements on the Z resonance*, *Phys. Rept.* **427** (2006) 257–454, [[hep-ex/0509008](#)].
- [69] A. Sopczak, *Search for new particles at LEP*, *Acta Phys. Polon. B* **30** (1999) 3229–3245, [[hep-ph/9911445](#)].
- [70] CMS collaboration, A. Tumasyan et al., *Inclusive nonresonant multilepton probes of new phenomena at $\sqrt{s}=13$ TeV*, *Phys. Rev. D* **105** (2022) 112007, [[2202.08676](#)].

[71] ATLAS collaboration, G. Aad et al., *Search for third-generation vector-like leptons in pp collisions at $\sqrt{s} = 13$ TeV with the ATLAS detector*, *JHEP* **07** (2023) 118, [[2303.05441](#)].

[72] CMS collaboration, V. Chekhovsky et al., *Search for vector-like leptons with long-lived particle decays in the CMS muon system in proton-proton collisions at $\sqrt{s} = 13$ TeV*, *JHEP* **08** (2025) 156, [[2503.16699](#)].

[73] C.-Y. Chen, S. Dawson and E. Furlan, *Vectorlike fermions and Higgs effective field theory revisited*, *Phys. Rev. D* **96** (2017) 015006, [[1703.06134](#)].

[74] PARTICLE DATA GROUP collaboration, S. Navas et al., *Review of particle physics*, *Phys. Rev. D* **110** (2024) 030001.

[75] MUON g-2 collaboration, D. P. Aguillard et al., *Measurement of the Positive Muon Anomalous Magnetic Moment to 127 ppb*, *Phys. Rev. Lett.* **135** (2025) 101802, [[2506.03069](#)].

[76] MUON g-2 collaboration, G. W. Bennett et al., *Final Report of the Muon E821 Anomalous Magnetic Moment Measurement at BNL*, *Phys. Rev. D* **73** (2006) 072003, [[hep-ex/0602035](#)].

[77] R. Aliberti et al., *The anomalous magnetic moment of the muon in the Standard Model: an update*, *Phys. Rept.* **1143** (2025) 1–158, [[2505.21476](#)].

[78] A. Alloul, N. D. Christensen, C. Degrande, C. Duhr and B. Fuks, *FeynRules 2.0—a complete toolbox for tree-level phenomenology*, *Computer Physics Communications* **185** (Aug., 2014) 2250–2300.

[79] C. Degrande, C. Duhr, B. Fuks, D. Grellscheid, O. Mattelaer and T. Reiter, *UFO - The Universal FeynRules Output*, *Comput. Phys. Commun.* **183** (2012) 1201–1214, [[1108.2040](#)].

[80] J. Alwall, R. Frederix, S. Frixione, V. Hirschi, F. Maltoni, O. Mattelaer et al., *The automated computation of tree-level and next-to-leading order differential cross sections, and their matching to parton shower simulations*, *Journal of High Energy Physics* **2014** (July, 2014) .

[81] C. Bierlich et al., *A comprehensive guide to the physics and usage of PYTHIA 8.3*, *SciPost Phys. Codeb.* **2022** (2022) 8, [[2203.11601](#)].

[82] T. H. Park, *Jet energy resolution measurement of the atlas detector using momentum balance*, Oct., 2018.

[83] CMS collaboration, V. Khachatryan et al., *Jet energy scale and resolution in the CMS experiment in pp collisions at 8 TeV*, *JINST* **12** (2017) P02014, [[1607.03663](#)].

[84] I. Pezzotti et al., *Dual-Readout Calorimetry for Future Experiments Probing Fundamental Physics*, [2203.04312](#).

[85] M. Cacciari, G. P. Salam and G. Soyez, *The anti- k_T jet clustering algorithm*, *JHEP* **04** (2008) 063, [[0802.1189](#)].

[86] M. Cacciari, G. P. Salam and G. Soyez, *FastJet User Manual*, *Eur. Phys. J. C* **72** (2012) 1896, [[1111.6097](#)].

[87] J. M. Butterworth, A. R. Davison, M. Rubin and G. P. Salam, *Jet substructure as a new Higgs search channel at the LHC*, *Phys. Rev. Lett.* **100** (2008) 242001, [[0802.2470](#)].

[88] S. Bentvelsen and I. Meyer, *The Cambridge jet algorithm: Features and applications*, *Eur. Phys. J. C* **4** (1998) 623–629, [[hep-ph/9803322](#)].

[89] G. Cowan, K. Cranmer, E. Gross and O. Vitells, *Asymptotic formulae for likelihood-based tests of new physics*, *Eur. Phys. J. C* **71** (2011) 1554, [[1007.1727](#)].

- [90] N. Kumar and S. P. Martin, *Vectorlike Leptons at the Large Hadron Collider*, *Phys. Rev. D* **92** (2015) 115018, [[1510.03456](#)].
- [91] P. N. Bhattiprolu, S. P. Martin and J. D. Wells, *Criteria for projected discovery and exclusion sensitivities of counting experiments*, *Eur. Phys. J. C* **81** (2021) 123, [[2009.07249](#)].